ADVANCED POWDER TECHNOLOGY

[The Society of Powder Technology, Japan, No. 5 Bldg., 181 Kitamachi, Karasuma-dori Rokujo-agaru, Simogyo-ku, Kyoto 606-8176 Japan]

PUBLISHER: ELSEVIER

Editor-in-Chief: Professor Dr. Shuji Matsusaka, Department of Chemical Engineering, Kyoto University, Kyoto, Japan.

ISSN: 0921-8831; IMPACT FACTOR= 2.659

Accepted December 12th 2017

JOULE HEATING AND BUOYANCY EFFECTS IN ELECTRO-OSMOTIC PERISTALTIC TRANSPORT OF AQUEOUS NANOFLUIDS THROUGH A MICROCHANNEL WITH COMPLEX WAVE PROPAGATION

^[1]Dharmendra Tripathi, [1]Ashish Sharma and **[2]O. Anwar Bég**

[1]Department of Mechanical Engineering, Manipal University Jaipur, Rajasthan-303007, India.

[2] Fluid Dynamics, Bio-Propulsion and Nanosystems, Department of Mechanical and Aeronautical Engineering, Salford University, Newton Building, Salford, M54WT, England, UK.

***^Corresponding Author**: D. Tripathi (dharmendra.tripathi@jaipur.manipal.edu)*

ABSTRACT

Electro-osmotic peristaltic transport of aqueous nanofluids in a two-dimensional micro-channel is examined analytically. Such flows arise in bio-mimetic pumping systems at the very small scale of interest in physiological treatment e.g. occular drug delivery systems. Complex waveforms are imposed at the walls to mimic sophisticated peristaltic wave propagation scenarios. Nano-particles are assumed to be in local thermal equilibrium. Joule electro-thermal heating is included. The dimensional conservation equations are linearized and transformed from the wave to the fixed (laboratory) frame under lubrication theory approximations. The emerging dimensionless model features a number of important thermo-physical, electrical and nanoscale parameter, namely thermal and solutal (basic density) Grashof numbers, nanoscale Brownian motion parameter, thermophoresis parameter, Helmholtz-Smoluchowski velocity (maximum electro-osmotic velocity), Debye electrokinetic length and Joule heating to surface heat flux ratio. Closed-form solutions are derived for the nano-particle volume fraction, temperature, axial velocity, averaged volumetric flow rate, pressure difference across one wavelength, skin friction (wall shear stress function), Nusselt number (wall heat transfer rate) and stream function distribution in the wave frame. The influence of selected parameters on these flow variables is studied with the aid of graphs. Bolus formation is also visualized and streamline distributions are observed to be strongly influenced and asymmetric in nature.

KEYWORDS: *Nano-particles; buoyancy; electro-kinetics; peristaltic waves; Debye length; heat transfer; Joule heating; Nusselt number; ocular drug delivery.*

1. INTRODUCTION

Nanofluids constitute suspensions of nanometer-sized particles in base fluids. In the medical context, many different nanoparticles have been explored in clinical applications, ranging from single-walled (SWCNT) and multi-walled carbon nanotubes, to metal oxides (gold, silver, titanium, copper etc.) and fullerene. The bio-compatibility [1] of nanofluids has led to their significant deployment in diverse areas of biomedical technologies including enzymes [2], anti-bacterial wound treatment [3], solid lipid and dendrimer nanofluids in ophthalmic [4-6], hypothermia regulation [7], radiofrequency ablation in cancer care [8] and orthopedic lubrication [9]. The effectiveness of nano-particle doping of fluids was first demonstrated by Choi [10] wherein it was shown that thermal conductivity characteristics of base fluids (e.g. silicon oil, ethylene glycol etc) and other features may be enhanced with metallic nano-particles. Following experimental investigations, two major theoretical approaches to simulating volume-averaged properties of nanofluids have emerged. The Buongiorno MIT model [11] emphasizes the contribution of Brownian diffusion and thermophoresis for heat transfer enhancement applications. The Tiwari-Das formulation [12] features a nano-particle volume fraction and allows the simulation of different types of nano-particles. In the former [11] a separate mass (species) diffusion equation in addition to momentum and heat conservation equations is required whereas in the latter [12] only momentum and energy conservations equations are considered. Both models have been deployed extensively in medical engineering for formulating boundary value problems and circumvent the need for conducting very costly numerical simulations of nano-particle interactions which require the use of direct numerical simulation, Lattice Boltzmann methods etc. Latiff *et al.* [13] used Maple symbolic software to study the transient nano-bio-polymeric flow from an extending/contracting sheet. Tan *et al*. [14] used both an immersed finite element method and Brownian adhesion dynamics algorithm to simulate the interaction of nano-particles with deforming red blood cells (RBCs) in drug delivery. Gentile *et al.* [15] studied analytically the longitudinal transport of nanoparticles in intra-vascular blood vessels using the Taylor-Aris dispersion model and Casson viscoplastic theory for blood. Bég *et al*. [16] used a Nakamura finite difference algorithm to study the bioconvection flow in nanofluids through deformable channels as a model of nanotechnological

microbial fuel cells. Tan *et al.* [17] studied fluid-structure interaction aspects of nano-particle diffusion in vascular networks with a combined particulate and continuum model, also addressing particulate ligand–receptor binding kinetics. Bég *et al*. [18] presented a computational simulations to study multiple aluminum oxide nano-particle transport in cylindrical vessels with a single-phase model and three different two-phase models (volume of fluid (VOF), mixture and Eulerian), observing that two-phase models correlate more closely with experimental measurements. Tan *et al*. [19] applied a Lattice Boltzmann-immersed boundary method to simulate nano-particle dispersion in blood vessels, confirming that dispersion rate is strongly influenced by local disturbances in the flow due to RBC motion and deformation.

Peristalsis is a significant mechanism encountered in many complex biological transport processes. It utilizes deformability of the conveying vessel to generate contracting and expanding waves which propel contents very efficiently over large distances and through tortuous paths. An excellent appraisal of the fluid dynamics of peristalsis has been presented by Jaffrin and Shapiro [20] for two-dimensional Newtonian flows. Applications of peristalsis arise in arthropumps [21] (which combine peristaltic and pulsatile i.e. periodic flow), piezoelectric actuated micro-pumps [22], swallowing mechanisms [23], waste management pumping systems [24] and also in geophysical (coastal) processes [25]. Extensive analytical investigations of peristaltic pumping flows have been communicated over a number of decades. Wilson and Pattin [26] studied peristalsis in two-dimensional conduits, observing that a lateral bending wave propagating along the walls of the channel generates a mean flow. Gupta and Shehadri [27] considered peristaltic wave propagation in viscous incompressible flow in non-uniform conduits. Ishikawa *et al*. [28] studied numerically the microbial flora transport in peristaltic flow in gastrointestinal tract, noting that viscous effects and wave amplitude significantly influence bacterial population and also concentration distributions of oxygen and nutrient. These studies did not consider nanofluid pumping by peristalsis. Bég and Tripathi [29] probably presented the first mathematical study of peristaltic transport of nanofluids in two-dimensional channels. They explored in detail the influence of cross-diffusion (Soret and Dufour) effects and also Brownian motion and thermophoresis on pressure difference distributions and streamline evolution. More recently Akbar *et al.*

[30] used Mathematica symbolic software and a Chebyschev spectral collocation method to study the effects of various nanoparticle geometries (bricks, cylinders and platelets) on magnetized peristaltic nanofluid dynamics with heat transfer in a vertical channel. They noted that temperature is enhanced significantly for brick-shaped nanoparticles. Electroosmotic flow (EOF) refers to the electrically-driven transport of a fluid relative to the stationary charged surfaces which bound it, for example micro-channel walls. It has substantial benefits in microfluidic pumping and allows very effective regulation of micro-channel flow fields via electric fields since it does not require the customary moving components featured in conventional micro-pumps. Electro-osmotic pumping has been observed to produce a continuous pulse-free flow. These pumps are also much more amenable to fabrication at the microscale and are increasingly being deployed in biomedical systems including pharmacological delivery, plasma separation, electro-osmotically actuated bio-microfluidic systems etc. Essentially flow actuation is achieved by applying an electric field to an electrolyte in contact with a surface. The contact of the surface with the electrolyte results in a net charge density in the solution. The viscous drag causes the liquid to flow tangentially to the surface and produces a consistent net migration of ions. Many theoretical and computational studies electro-osmotic flow with and without heat transfer have been reported. Babaie *et al.* [31] studied numerically with a finite difference method the fully developed electroosmotic flow of power-law fluids via a slit microchannel with a constant wall heat flux boundary condition, noting that both zeta potential and non-Newtonian behavior strongly modify heat transfer rate and volumetric flow rate at low values of the dimensionless Debye-Hückel parameter. Hu *et al.* [32] presented both particle-based numerical and current-monitoring laboratory results for electro-osmotic flow through microchannels with 3D prismatic elements. Masilamani et al. [33] used Lattice Boltzmann and finite difference algorithms to analyse the non-Newtonian electro-osmotic flow in micro-channels, noting the significant modification in flow patterns with rheological effects.Sadeghi *et al*. [34] used a power-series analytical method to derive solutions for the fully developed electroosmotic slip flow in hydrophobic microducts of general cross section under the Debye–Hückel approximation, considering many different microgeometries (e.g. trapezoidal, double-trapezoidal, isosceles triangular, rhombic, elliptical, semi-elliptical, rectangular etc), They

showed that flow rate increases in a linear fashion with slip length for thinner electric double layers (EDLs) Liao *et al.* [35] employed a finite element Galerkin algorithm to compute the mixed electro-osmotic/pressure-driven flows in triangle microchannels by solving the Poisson and Naiver–Stokes equations, highlighting that electrolytic solution mass flux is enhanced with positive pressure gradient and Debye length ratio. Marcos *et al.* [36] used a control volume integration method to simulate the steady state developing electro-osmotic flow in closed-end cylindrical micro-channels computing in detail the influence of electric field strength and channel geometry on pressure and velocity fields. These studies generally neglected the contribution of *Joule heating (dissipation).* This phenomenon relates to the heat generated from the electrical current arising from the flowing liquid with net free charges, which is common for the electro-osmotic flows at the micro/nanoscale. It is therefore a significant effect to consider in biomicrofluidics systems simulations since it may impact considerably on both pumping rates and wall heat transfer rates since it produces temperature gradients in cross-stream and axial directions which can alter the applied electric potential field and the flow field. Inclusion of Joule heating in mathematical EOF models therefore circumvents *over-prediction* of micro-pump characteristics. Bosse and Arce [37] investigated the influence of Joule dissipation on solute dispersion in a free convection electrophoretic cell for the batch mode of operation. Xuan and Li [38] investigated analytically the impact of Joule heating effects on the transport of heat, electricity, momentum and mass species in capillary-based electrophoresis, showing that the thermal end effect induces significant depletion in temperature close to capillary ends, and that in these zones higher electric field strengths are necessary to ensure current continuity. Jing et al. [39] studied theoretically the Joule heating and viscous dissipation effects in steady, laminar, hydrodynamically and thermally fully developed pressure-driven flow in a microchannel with surface charge-dependent slip. They found that Joule heating and viscous dissipation demonstrate a non-monotonic variation with the continually increasing zeta potential and that owing to deceleration in the flow there is an associated decrease in Nusselt number with zeta potential. Further studies have been communicated by Yavari *et al*. [40] who considered non-uniform Joule heating and variable thermophysical property effects for EO dynamics in microtubes noting that a reduction in electrical resistivity of the fluid by increasing

temperature elevates the total energy generation due to the Joule heating and manifests in a decrease in Nusselt number. Several studies have also examined the combined *peristaltic pumping* of electro-osmotic flow and heat transfer in micro-channels with Joule heating effects. Recently Sutradhar *et al.* [41] presented perturbation solutions for electro-magnetic peristaltic transport of Casson blood in a permeable microvessel and observed that temperature is amplified with greater Joule heating. Nanofluid peristaltic pumping with Joule heating was analyzed by Hayat *et al.* [42] who also considered viscoelastic characteristics, wall slip and radiative heat transfer effects. Very recently Tripathi *et al.* [43] presented analytical solutions for peristaltic transport of electro-osmotic nanofluids in finite micro-channels with Joule heating effects. This model however did not consider *Brownian motion* and *thermophoresis* effects as reflected in the Buongiorno formulation [11] and was also restricted to *axi-symmetric* pumping (the same peristaltic waves imposed at both micro-channel walls). In the present article, a generalized nanofluid model is employed to study more comprehensively the electro-osmotic flow and heat transfer in two-dimensional micro-channels with Joule heating. Furthermore complex waveforms are imposed at the micro-channel walls to consider *asymmetric* peristaltic pumping. The computations are relevant to more realistic designs for ocular electro-osmotic pumps in drug delivery systems.

2. MATHEMATICAL MODEL

We consider electro-osmotic transport of nanofluids through a complex wavy two-dimensional microchannel with Joule dissipation. The geometry of the channel is illustrated in **Fig.1** and mathematically expressed as:

$$\bar{h}(\bar{x},\bar{t}) = a + \sum_{i=1}^{m} \bar{\phi}_i \sin\frac{2i\pi}{\lambda}(\bar{x} - c\bar{t}) \quad , \tag{1}$$

where $\bar{h}, \bar{x}, \bar{t}, a, \bar{\phi}_i, \lambda$ and c represent transverse vibration of the wall, axial coordinate, time, half width of the channel, amplitude of the different (m) waves, wavelength and wave velocity respectively. The temperatures and nanoparticle volume fraction at the center line and the walls of the micro-channel are given as: $T = T_0, F = F_0$ (at $y = 0$), $T = T_1, F = F_1,$ (at $y = h$). Furthermore, a and $\bar{\phi}_i$ satisfy the condition: $a \le \sum_{i=1}^{n} \bar{\phi}_i$.

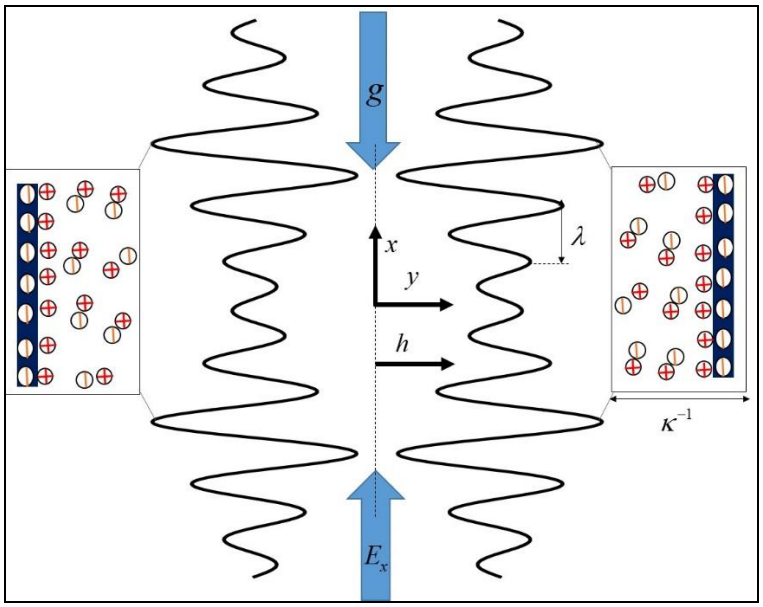

Fig.1. Schematic view of electro-osmotic peristaltic transport of nanofluids through a complex wavy microfluidic channel. Wave propagates with wave velocity c and with constant wavelength λ.

The equations governing the multi-physical flow problem are the mass (continuity), momentum, energy and nanoparticle fraction conservation equations:

$$\nabla.\mathbf{q} = 0, \tag{2}$$

$$\rho_f \left(\frac{\partial \mathbf{q}}{\partial \bar{t}} + (\mathbf{q}.\nabla)\mathbf{q} \right) = -\nabla \bar{p} + \mu \nabla^2 \mathbf{q} + \mathbf{f}_g + \bar{\rho}_e E_x, \tag{3}$$

$$(\rho c_p)_f \left(\frac{\partial \bar{T}}{\partial \bar{t}} + (\mathbf{q}.\nabla)\bar{T} \right) = k_{ef} \nabla^2 \bar{T} + (\rho c_p)_p D_b (\nabla \bar{F}.\nabla \bar{T}) + \frac{D_t}{T_0} (\nabla \bar{T}.\nabla \bar{T}) + \mu\varphi + \sigma E_x^2, \tag{4}$$

$$\frac{\partial \bar{F}}{\partial \bar{t}} + (\mathbf{q}.\nabla)\bar{F} = D_b \nabla^2 \bar{F} + \frac{D_t}{T_0} \nabla^2 \bar{T}, \tag{5}$$

where, $\mathbf{f}_g = g\left\{(1-F_0)\rho_0 \beta(\bar{T}-T_0) - (\rho_p - \rho_0)(\bar{F}-F_0)\right\}$, $\mathbf{q} \equiv (\bar{u}, \bar{v})$ is velocity vector, $\nabla \equiv i\frac{\partial}{\partial \bar{x}} + j\frac{\partial}{\partial \bar{y}}$ and $\nabla^2 = \nabla.\nabla \equiv \frac{\partial^2}{\partial x^2} + \frac{\partial^2}{\partial y^2}$ are Hamilton operator and Laplace operator respectively. The quantities $\rho_f, \bar{p}, \mu, \bar{\rho}_e, E_x, (\rho c_p)_f, (\rho c_p)_p, \rho_0, \rho_p, g, \beta, \bar{T}, \bar{F}, k_{ef}, \sigma,$

φ, D_t, D_b are the fluid density, pressure, viscosity, electrical charge density, applied axial electrical field, heat capacity of fluid, effective heat capacity of nanoparticle, the nanofluid density at the reference temperature (T_0), nanoparticle mass density, acceleration due to gravity, volumetric expansion coefficient of the fluid, temperature, nanoparticle volume fraction, thermal conductivity, electrical conductivity, viscous dissipation function, thermophoretic diffusion coefficient, Brownian diffusion coefficient respectively. The subscript f refers the fluid properties and p refers to nanoparticle properties. We introduce the following variables to non-dimensionalize the governing equations:

$x=\frac{\bar{x}}{\lambda},\ y=\frac{\bar{y}}{a},\ t=\frac{c\bar{t}}{\lambda},\ u=\frac{\bar{u}}{c},\ v=\frac{\bar{v}}{c\delta},\quad h=\frac{\bar{h}}{a},\ \ p=\frac{\bar{p}a^2}{\mu c\lambda},\ \phi_i=\frac{\bar{\phi}_i}{a},\Phi=\frac{\bar{\Phi}}{\zeta},n=\frac{\bar{n}}{n_0}.$ The nonlinear terms in the momentum equation are determined to be of $O\left(Re\,\delta^2\right)$, where $Re=\frac{\rho ca\delta}{\mu}$ is Reynolds number and $\delta=\frac{a}{\lambda}$ is the wave number. The relative order of volumetric heat generation due to electric resistance heating (Joule heating), and a local volumetric heating due to viscous dissipation, i.e. $R_v \sim \frac{\sigma a\mu}{\kappa\varepsilon^2\zeta^2}$, allows the neglection of viscous dissipation in comparison to Joule heating effects for channel widths greater than 10μm. Using lubrication theory and neglecting the viscous dissipation term, the governing equations for electro-osmotic nanofluid flow contract to:

$$\frac{\partial u}{\partial x}+\frac{\partial v}{\partial y}=0, \tag{6}$$

$$\frac{\partial p}{\partial x}=\frac{\partial^2 u}{\partial y^2}+Gr_t T-Gr_f F+U_{HS}\frac{\partial^2\Phi}{\partial y^2}, \tag{7}$$

$$\frac{\partial^2 T}{\partial y^2}+N_b\frac{\partial T}{\partial y}\frac{\partial F}{\partial y}+N_t\left(\frac{\partial T}{\partial y}\right)^2+S=0, \tag{8}$$

$$\frac{\partial^2 F}{\partial y^2}+\frac{N_t}{N_b}\frac{\partial^2 T}{\partial y^2}=0, \tag{9}$$

where, $Gr_t = \frac{\beta g \rho_0{}^2 a^3 (1-F_0)(T_1-T_0)}{\mu^2}$ and $Gr_f = \frac{g\rho_0 a^3(\rho_p-\rho_0)(F_1-F_0)}{\mu^2}$ are the thermal Grashof number and basic-density (nano-particle solutal) Grashof number, $N_b = \frac{(\rho c_p)_p D_b (F_1-F_0)}{k}$ and $N_t = \frac{(\rho c_p)_p D_t (T_1-T_0)}{kT_0}$ are Brownian motion parameter and thermophoresis parameter, $T = \frac{\bar{T}-T_0}{T_1-T_0}$ and $F = \frac{\bar{F}-F_0}{F_1-F_0}$ are the dimensionless temperature and nanoparticle volume fraction, $U_{HS} = -\frac{E_x \varepsilon \zeta}{\mu c}$ is the Helmholtz-Smoluchowski velocity or maximum electro-osmotic velocity, ζ is zeta potential, and $S = \sigma E_x^2 a^2 / k_{ef}(T_1-T_0)$, is the normalized generation term that represents the ratio of Joule heating to surface heat flux (for constant wall temperature conditions). The Poisson-Boltzmann equation for $\zeta < 25\text{mV}$, is expressed as $\frac{\partial^2 \Phi}{\partial y^2} = \kappa^2 \Phi$, where $\kappa = aez\sqrt{\frac{2n_0}{\varepsilon K_B T}}$ is the Debye-Hückel parameter which is the *inverse* of Debye length, ε is the electrical permittivity of the electrolytic nanofluid, k_B is Boltzmann constant. Employing the boundary conditions: $\Phi_y(0) = 0$ and $\Phi(h) = 1$, the electrical potential function is obtained as:

$$\Phi = \frac{\cosh(\kappa y)}{\cosh(\kappa h)}. \tag{10}$$

The physical boundary conditions for temperature, nanoparticle volume fraction and velocity are imposed as:

$$T\big|_{y=0} = 0, T\big|_{y=h} = 1, F\big|_{y=0} = 0, F\big|_{y=h} = 1, \left.\frac{\partial u}{\partial y}\right|_{y=0} = 0, u\big|_{y=h} = 0, \tag{11}$$

Solving Eqns. (8) & (9) with boundary conditions (11), the *temperature field* and *nanoparticle volume fraction* are determined as:

$$T=\frac{1}{N}\left\{\frac{2e^{N}\sinh\left(\frac{Ny}{h}\right)(N+h^{2}S)}{(-1+e^{N})}-e^{\frac{Ny}{h}}hSy\right\}, \tag{12}$$

$$F=\frac{y}{N_b}\left(\frac{N}{h}+\frac{e^{\frac{Ny}{h}}hS}{N}\right)-\frac{2e^{N}(N+h^{2}S)\sinh\left(\frac{Ny}{h}\right)}{N_bN(-1+e^{N})}, \tag{13}$$

where, $N=N_b+N_t$.

Substituting Eqns. (12) & (13) into Eq.(7), further integrating and employing the boundary conditions of Eq.(11), leads to the following expression for *axial velocity*:

$$u=\frac{e^{-\frac{(Nb+Nt)y}{h}}}{6hNb(-1+e^{Nb+Nt})(Nb+Nt)^{3})}\left\{A_{11}e^{Nb+Nt}+A_{12}e^{\frac{(Nb+Nt)y}{h}}+A_{13}e^{\frac{(Nb+Nt)(h+y)}{h}}+A_{14}e^{\frac{(Nb+Nt)y}{h}}\right\}, \tag{14}$$

where, A_{11}, A_{12}, A_{13}, A_{14} are functions documented in the Appendix (Eqns. A7-A10).

The *volumetric flow rate* is defined as follows:

$$Q=\int_{0}^{h}udy. \tag{15}$$

The detailed expression is given in the Appendix (Eqn. A11)

The pressure difference across the one wavelength is defined as:

$$\Delta p=\int_{0}^{1}\frac{\partial p}{\partial x}dx, \tag{16}$$

where, $\frac{\partial p}{\partial x}$ is *axial pressure gradient* which again is provided in Appendix (Eqn. A12).

The transformations between the wave frame (x_w, y_w) moving with velocity (c) and the fixed frame (x, y) are given by :

$$x=x_w-t,\quad y=y_w,\quad u=u_w+1,\quad v=v_w, \tag{17}$$

where (u_w, v_w) and (u, v) are the velocity components in the wave and fixed frame respectively.

The *volumetric flow rate in the wave frame* is given by

$$q_w = \int_0^h u_w dy_w = \int_0^h (u-1) dy_w \,, \tag{18}$$

On integration this yields:

$$q_w = Q - h \,. \tag{19}$$

Averaging *volumetric flow rate along one time period*, we get:

$$\bar{Q} = \int_0^1 Q dt = \int_0^1 (q_w + h) dt \,, \tag{20}$$

which, on integration, yields

$$\bar{Q} = q_w + 1 = Q + 1 - h \,. \tag{21}$$

The stream function is defined as:

$$u_w = \frac{\partial \psi}{\partial y_w}, v_w = -\frac{\partial \psi}{\partial x_w} \,. \tag{22}$$

The skin friction coefficient (C_f), and Nusselt number (Nu) are defined as:

$$C_f = \left. \frac{\partial h}{\partial x} \frac{\partial u}{\partial y} \right|_{y=h} , \tag{23}$$

$$Nu = \left. \frac{\partial h}{\partial x} \frac{\partial \theta}{\partial y} \right|_{y=h} \,. \tag{24}$$

3. NUMERICAL RESULTS AND DISCUSSION

We have considered the wall deformation equation in non-dimensional form in the wave frame of reference as $h = 1 + \sum_{i=1}^{m} \phi_i \sin(2i\pi x)$, where, m is the number of waves propagating together. In all numerical computations, we take $m = 10$ and the values of amplitudes are taken as: $\phi_1 = 0.01, \phi_2 = 0.02, \phi_3 = 0.03, \phi_4 = 0.04, \phi_5 = 0.05, \phi_6 = 0.06, \phi_7 = 0.07, \phi_8 = 0.1, \phi_9 = 0.2, \phi_{10} = 0.3$, which satisfy the condition $1 \geq \sum_{i=1}^{m} \phi_i$ to avoid the interference of lower and upper walls. The influence of selected electro-osmotic, nanoscale and geometric parameters are visualized in **Figs. 2-9**. Both variations across the upper half space of the micro-channel (i.e. with the transverse *y*-coordinate) and in the axial direction (*x*-coordinate) are computed.

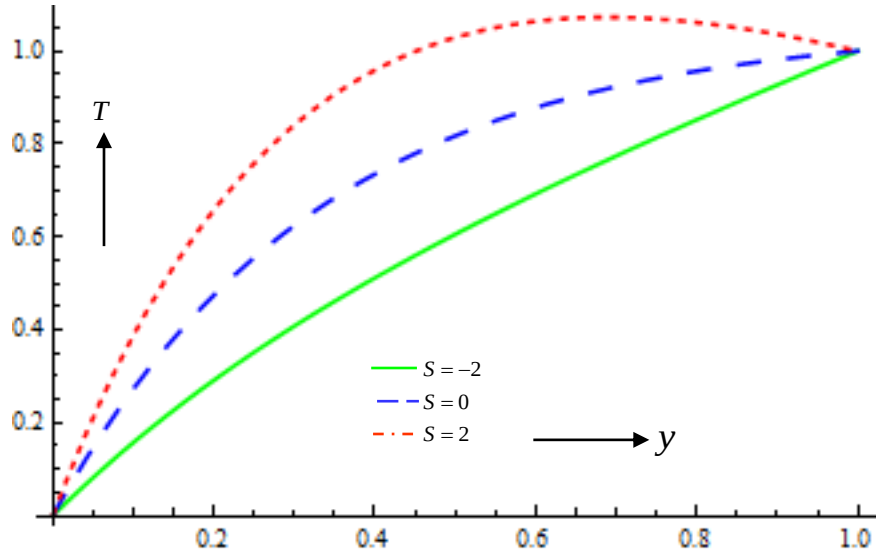

Fig.2. Temperature profile at $N_b = 1, N_t = 2$ for different values of Joule heating parameters.

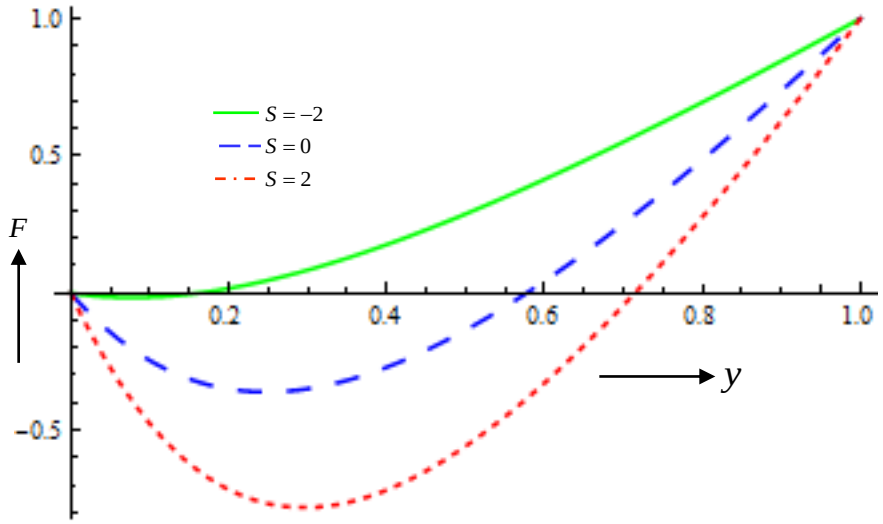

Fig.3. Nanoparticle volume fraction vs transverse coordinate at $N_b = 1, N_t = 2$ for different values of Joule heating parameters.

(a)

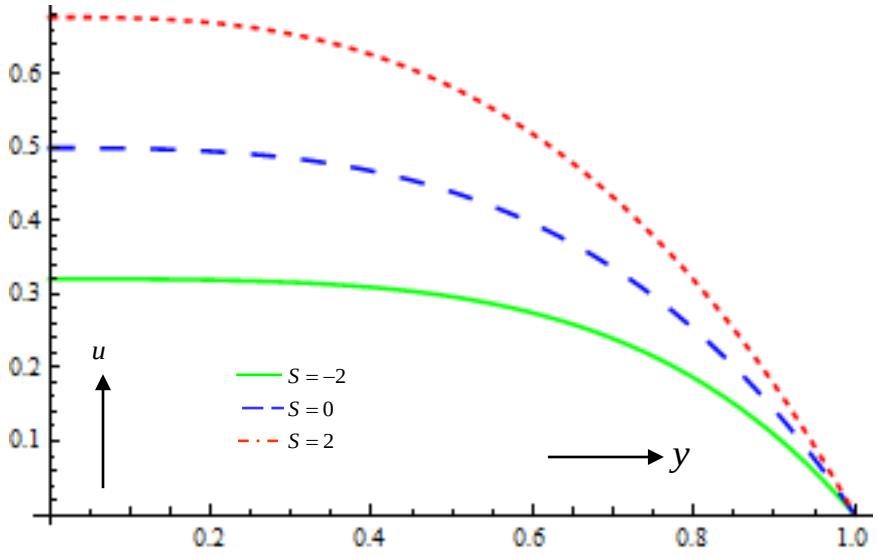
0.6
0.5
0.4
0.3
0.2
0.1
u
S = –2
S = 0
S = 2
y
0.2
0.4
0.6
0.8
1.0

(b)

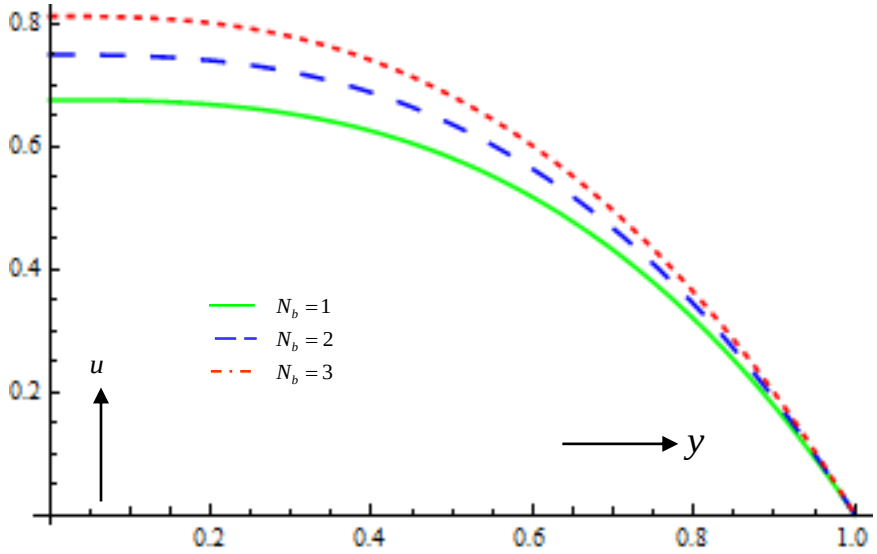
0.8
0.6
0.4
0.2
$N_b = 1$
$N_b = 2$
$N_b = 3$
u
y
0.2
0.4
0.6
0.8
1.0

(c)

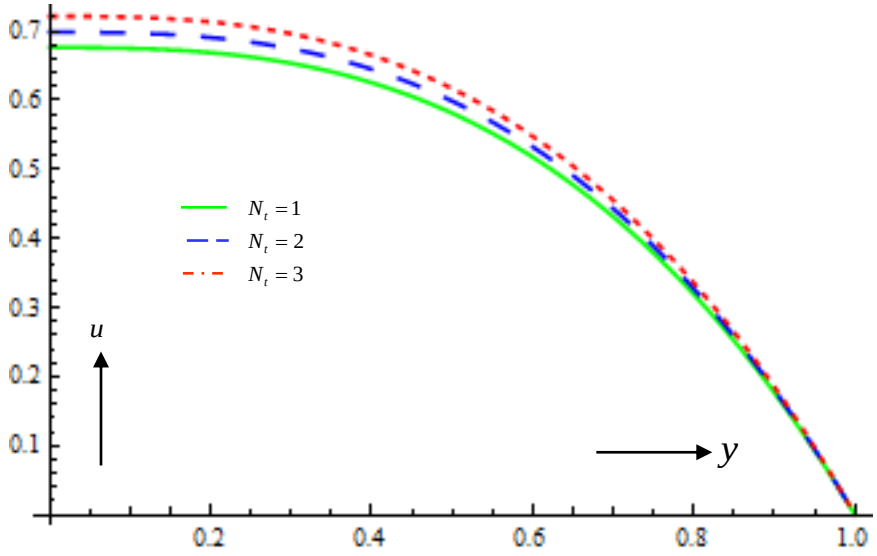
0.7
0.6
0.5
0.4
0.3
0.2
0.1
$N_t = 1$
$N_t = 2$
$N_t = 3$
u
y
0.2
0.4
0.6
0.8
1.0

(d)

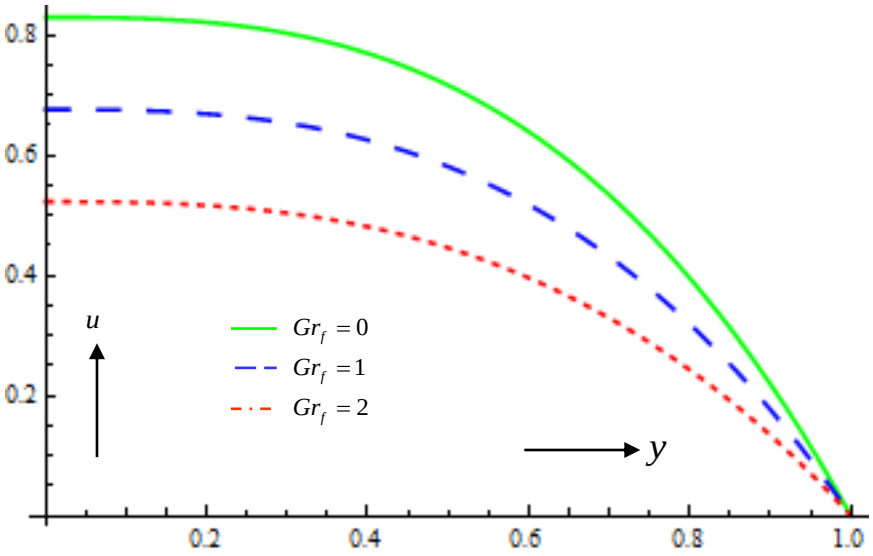
0.8
0.6
0.4
0.2
u
$Gr_f = 0$
$Gr_f = 1$
$Gr_f = 2$
y
0.2
0.4
0.6
0.8
1.0

(e)

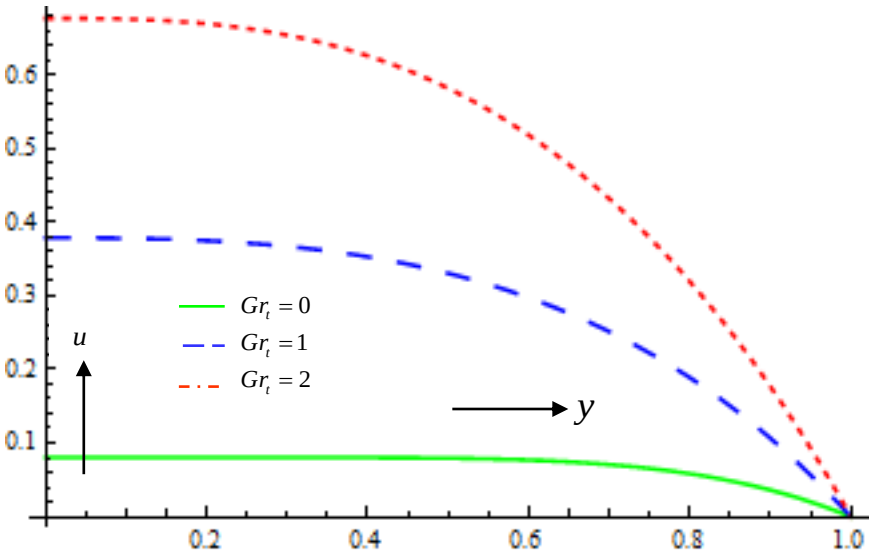
0.6
0.5
0.4
0.3
0.2
0.1
u
$Gr_t = 0$
$Gr_t = 1$
$Gr_t = 2$
y
0.2
0.4
0.6
0.8
1.0

(f)

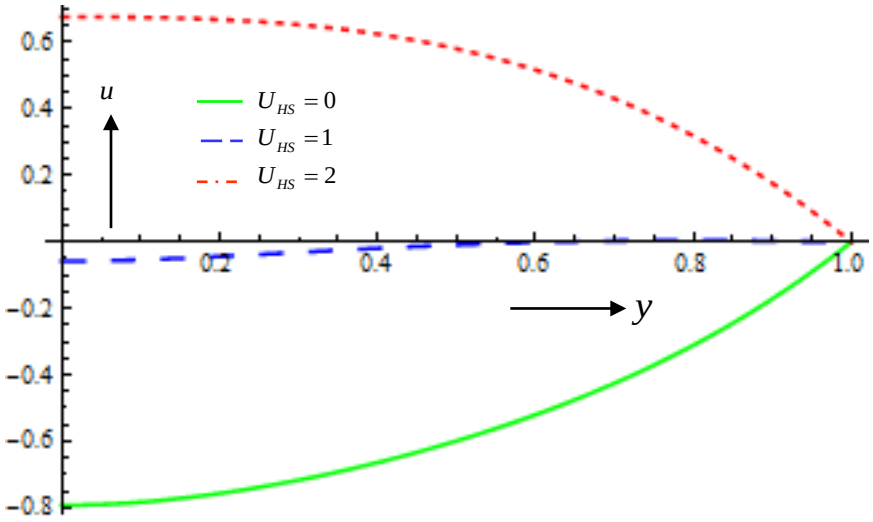
0.6
0.4
0.2
u
$U_{HS} = 0$
$U_{HS} = 1$
$U_{HS} = 2$
0.2
0.4
0.6
0.8
1.0
y
−0.2
−0.4
−0.6
−0.8

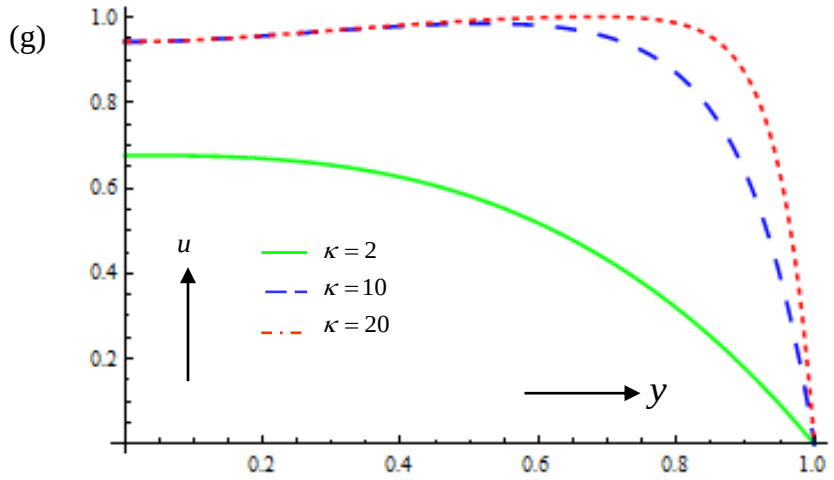

Fig.4. Velocity profile at $p_x = 1,$ for different values of (a) Joule heating parameters (b) Brownian motion parameter (c) thermophoresis parameter (d) basic-density Grashof number (e) thermal Grashof number (f) Helmholtz-Smoluchowski velocity (g) Debye–Hückel parameter.

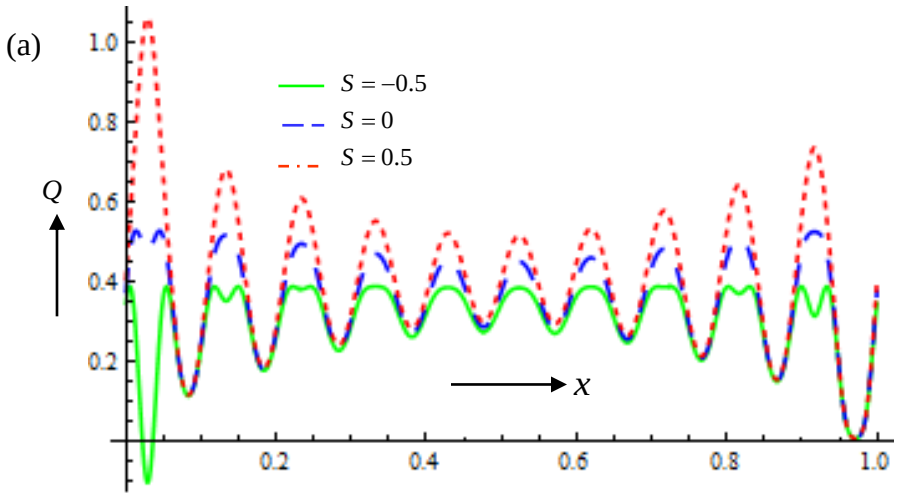

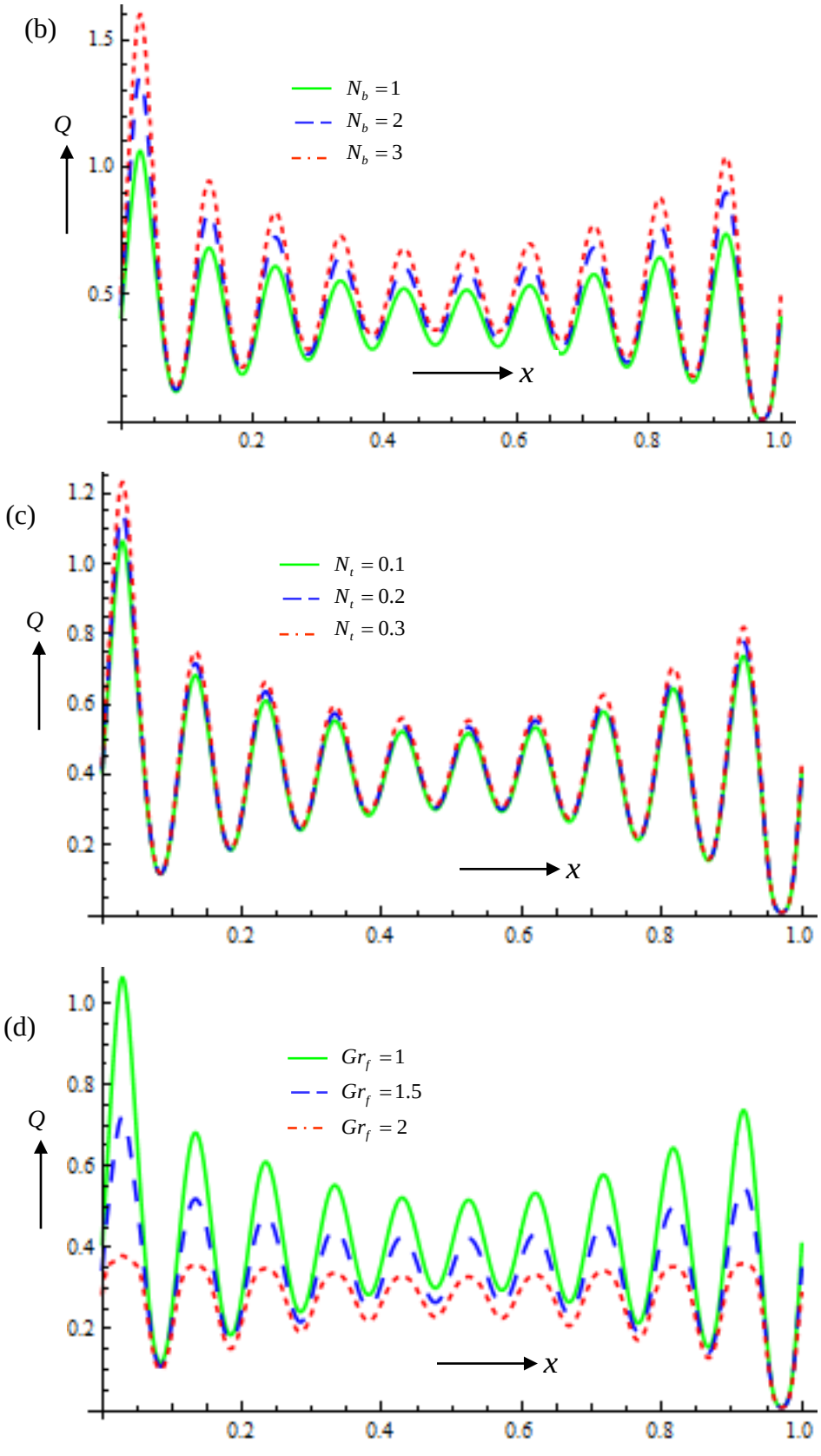
(b)
Q
x
$N_b = 1$
$N_b = 2$
$N_b = 3$
(c)
Q
x
$N_t = 0.1$
$N_t = 0.2$
$N_t = 0.3$
(d)
Q
x
$Gr_f = 1$
$Gr_f = 1.5$
$Gr_f = 2$

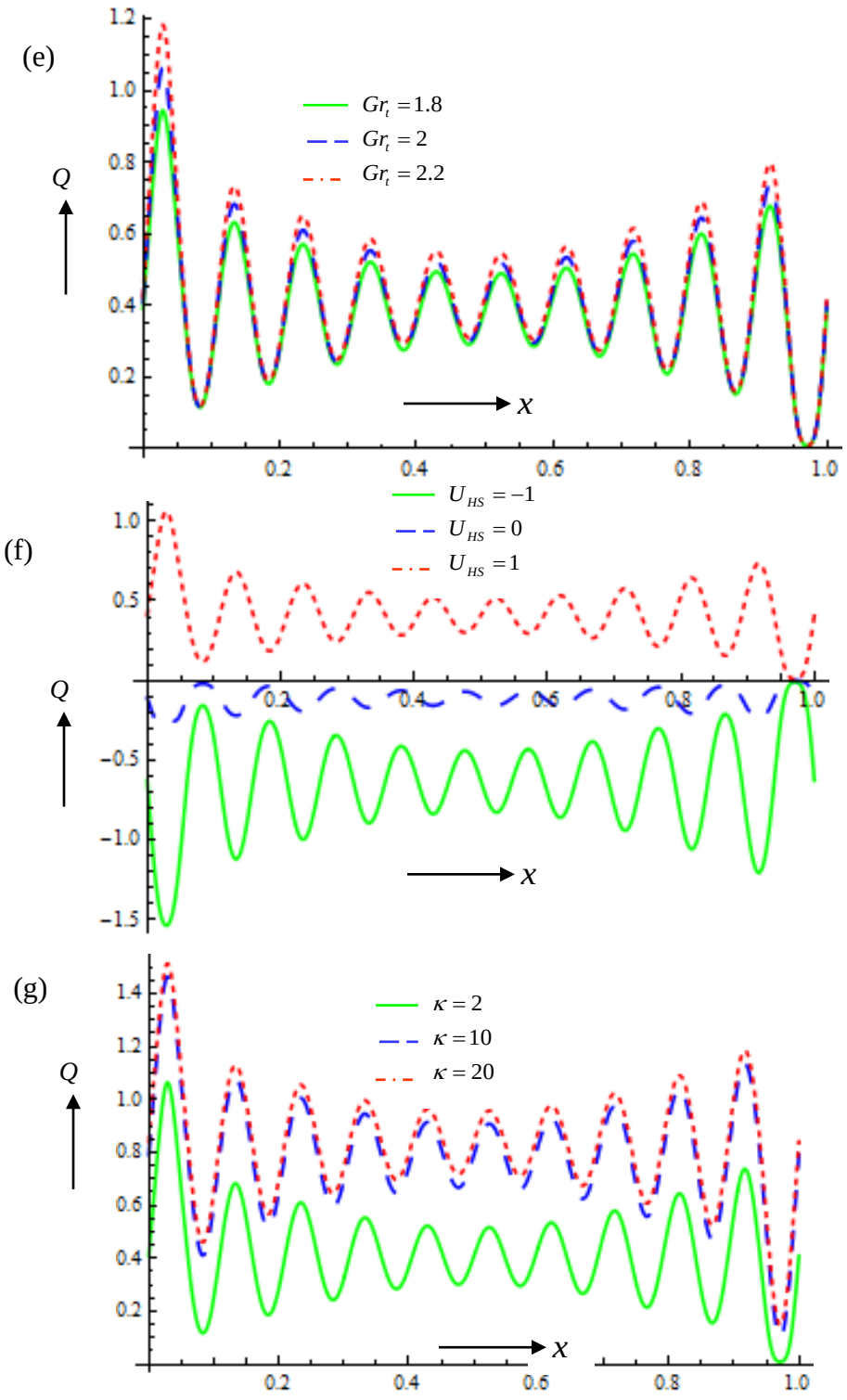

Fig.5. Volumetric flow rate along the channel length at $p_x = 1,$ for different values of (a) Joule heating parameters (b) Brownian motion parameter (c) thermophoresis parameter (d) basic-density Grashof number (e) thermal Grashof number (f) Helmholtz-Smoluchowski velocity (g) Debye–Hückel parameter.

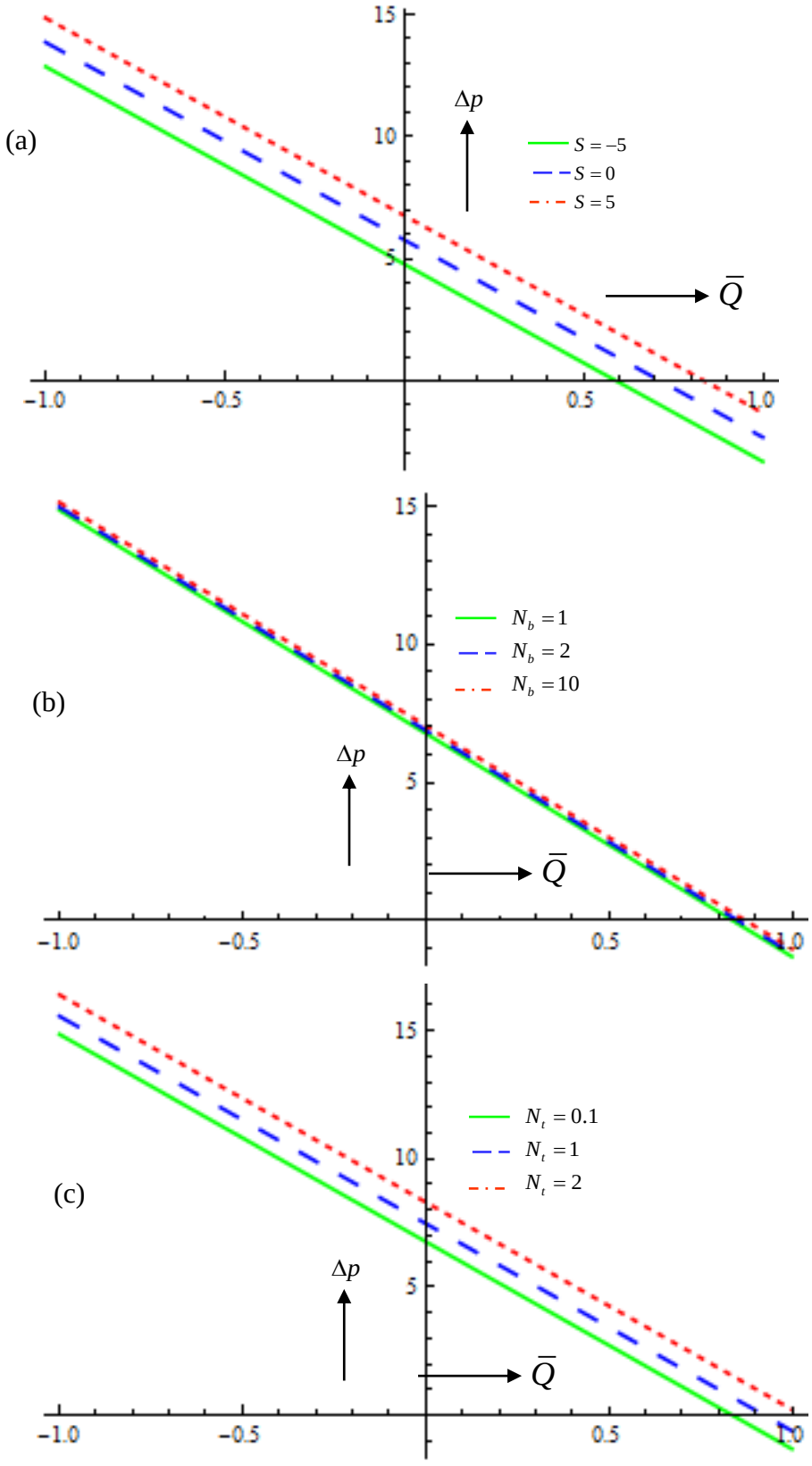
(a)
15
10
5
Δp
$\bar{Q}$
S = –5
S = 0
S = 5
–1.0
–0.5
0.5
1.0
(b)
$N_b = 1$
$N_b = 2$
$N_b = 10$
(c)
$N_t = 0.1$
$N_t = 1$
$N_t = 2$

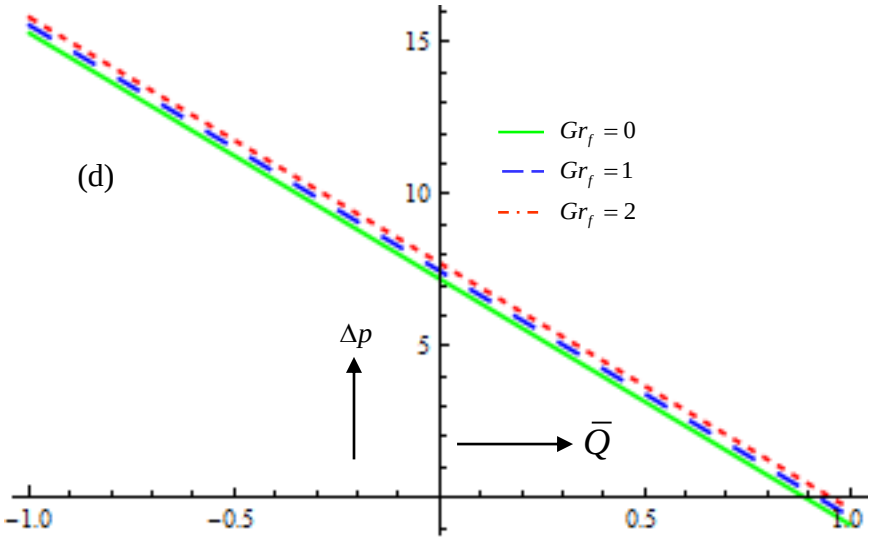
(d)
15
10
5
−1.0
−0.5
0.5
1.0
$Gr_f = 0$
$Gr_f = 1$
$Gr_f = 2$
Δp
$\bar{Q}$

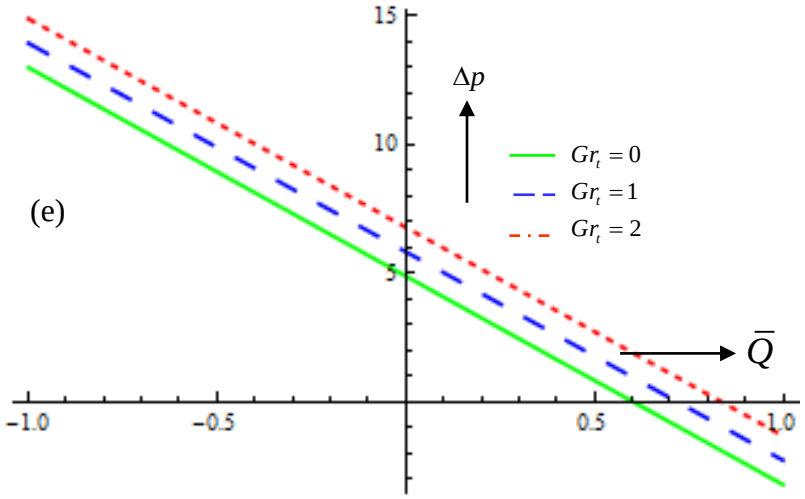
(e)
15
10
5
−1.0
−0.5
0.5
1.0
Δp
$Gr_t = 0$
$Gr_t = 1$
$Gr_t = 2$
$\bar{Q}$

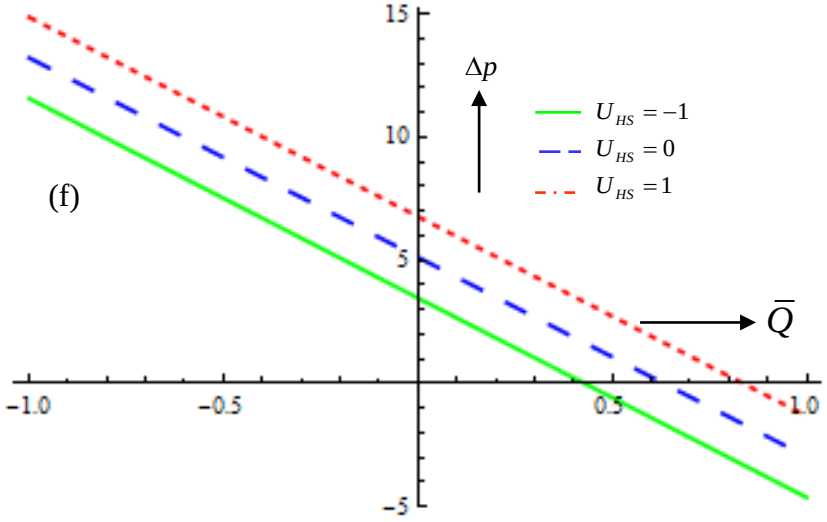
(f)
15
10
5
−5
−1.0
−0.5
0.5
1.0
Δp
$U_{HS} = -1$
$U_{HS} = 0$
$U_{HS} = 1$
$\bar{Q}$

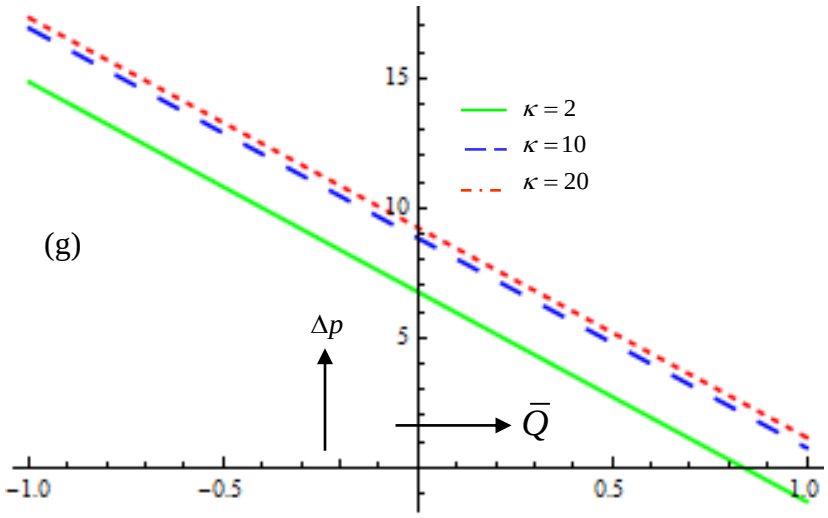

Fig.6. Pressure across one wavelength vs time averaged volumetric flow rate for different values of (a) Joule heating parameters (b) Brownian motion parameter (c) thermophoresis parameter (d) basic-density Grashof number (e) thermal Grashof number (f) Helmholtz-Smoluchowski velocity (g) Debye–Hückel parameter.

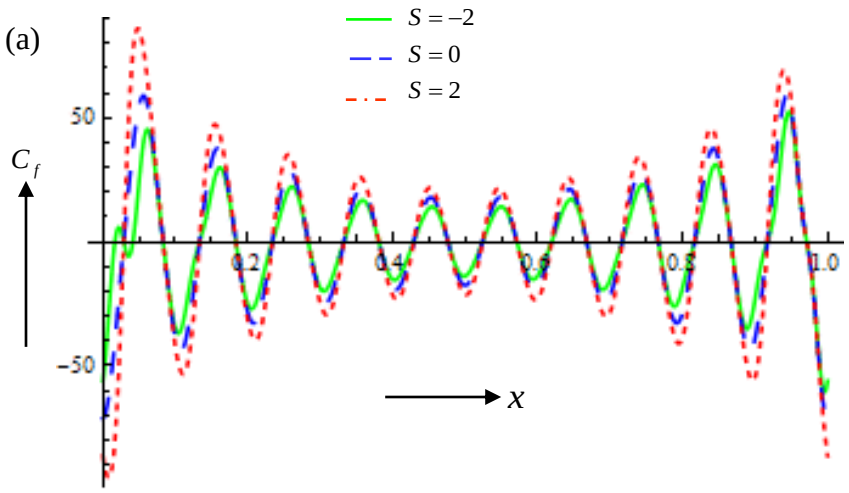

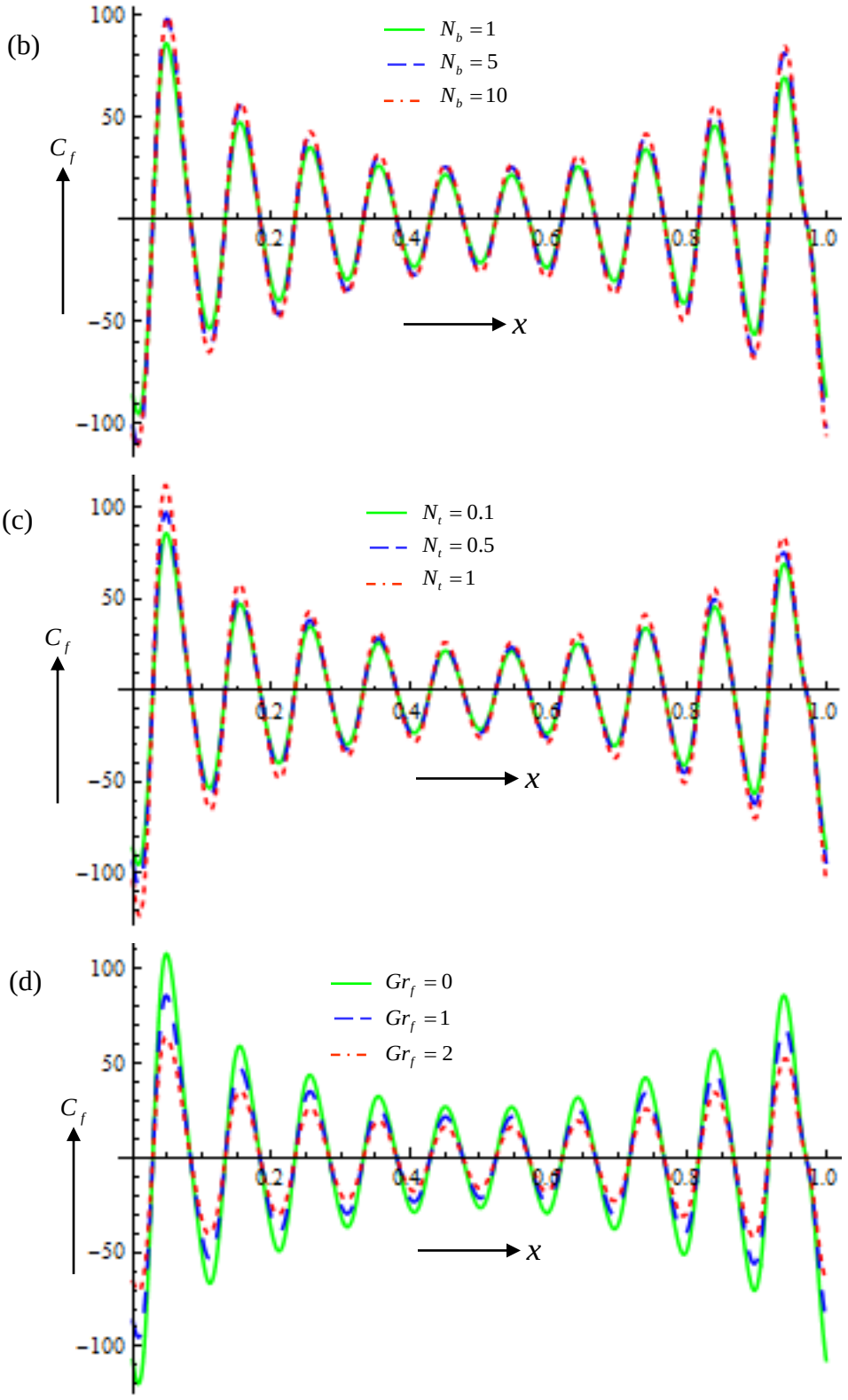
(b)
$N_b = 1$
$N_b = 5$
$N_b = 10$
C_f
x
100
50
−50
−100
0.2
0.4
0.6
0.8
1.0
(c)
$N_t = 0.1$
$N_t = 0.5$
$N_t = 1$
C_f
x
100
50
−50
−100
0.2
0.4
0.6
0.8
1.0
(d)
$Gr_f = 0$
$Gr_f = 1$
$Gr_f = 2$
C_f
x
100
50
−50
−100
0.2
0.4
0.6
0.8
1.0

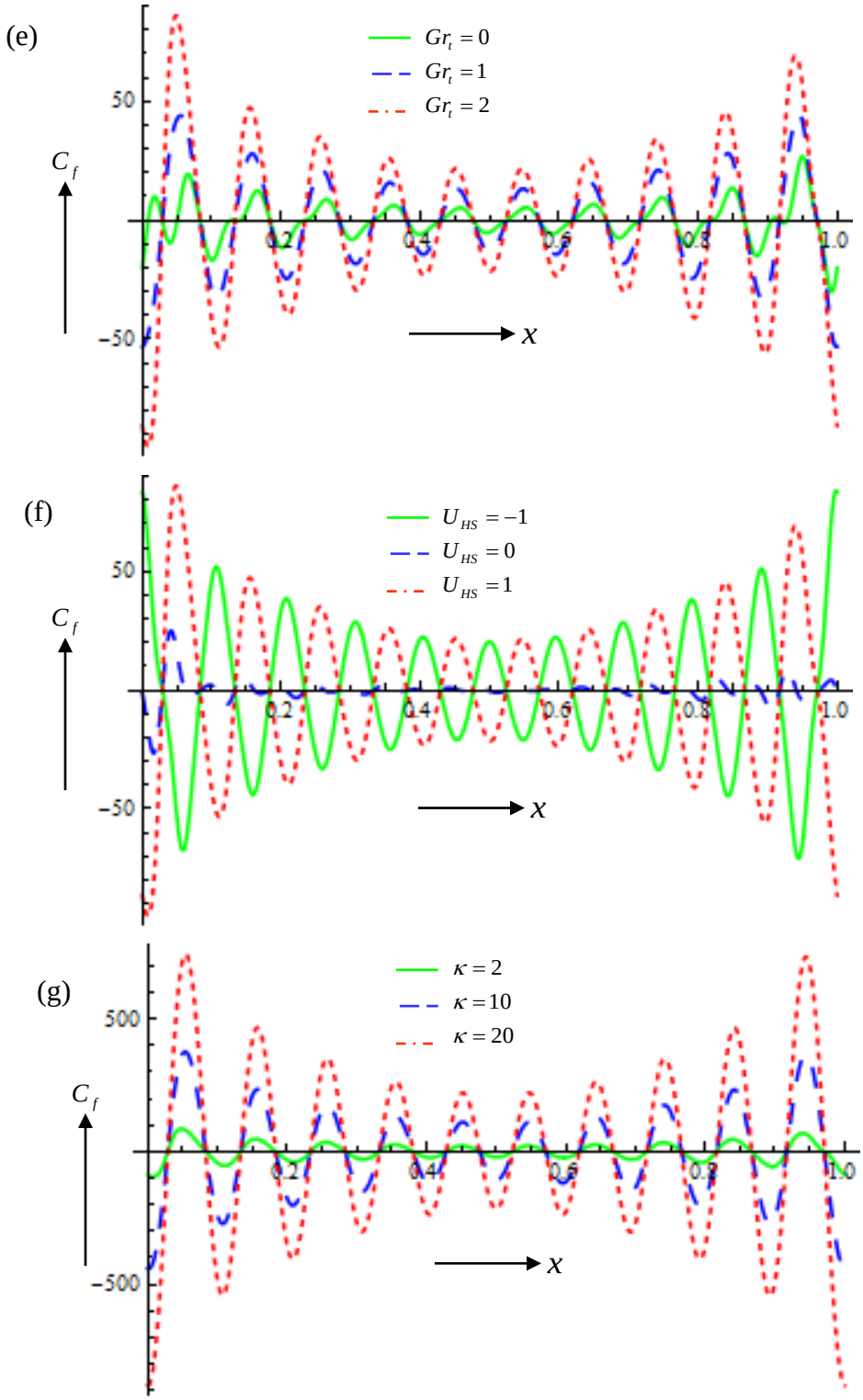

Fig.7. Skin friction coefficient along the channel length at $p_x = 1$, for different values of (a) Joule heating parameters (b) Brownian motion parameter (c) thermophoresis parameter (d) basic-density Grashof number (e) thermal Grashof number (f) Helmholtz-Smoluchowski velocity (g) Debye–Hückel parameter.

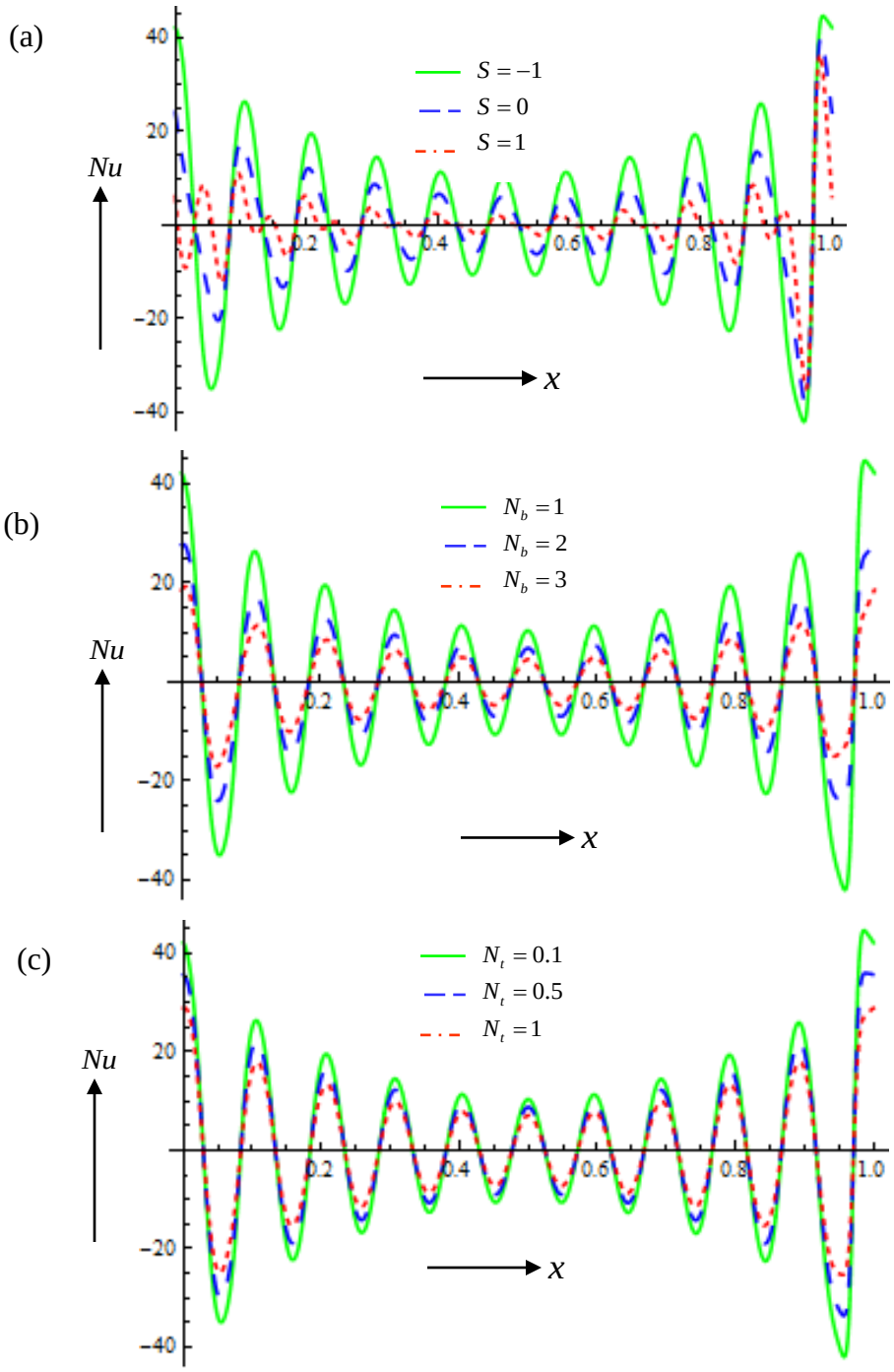

Fig.8. Nusselt number along the channel length at $p_x = 1$ for different values of (a) Joule heating parameters (b) Brownian motion parameter (c) thermophoresis parameter.

(a)

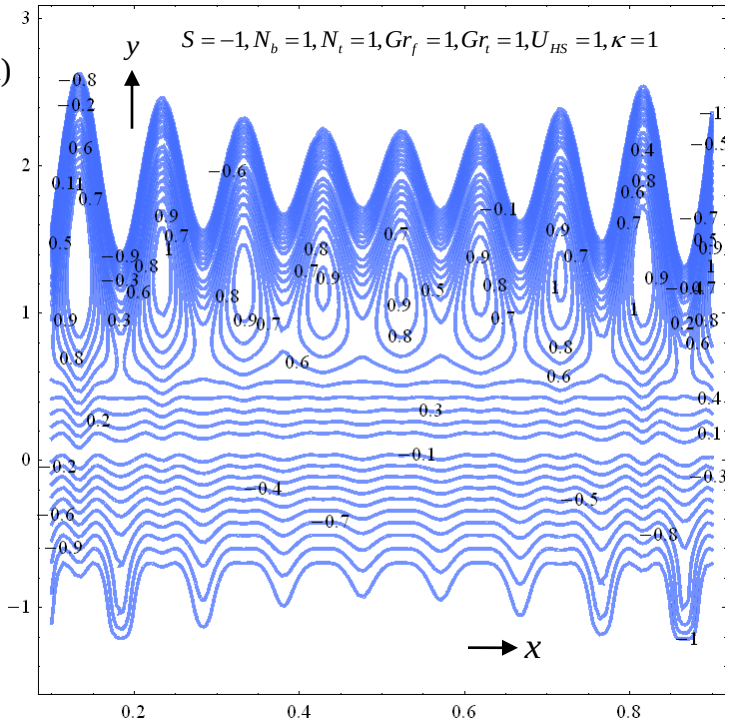
$S=-1, N_b=1, N_t=1, Gr_f=1, Gr_t=1, U_{HS}=1, \kappa=1$
y
x

(b)

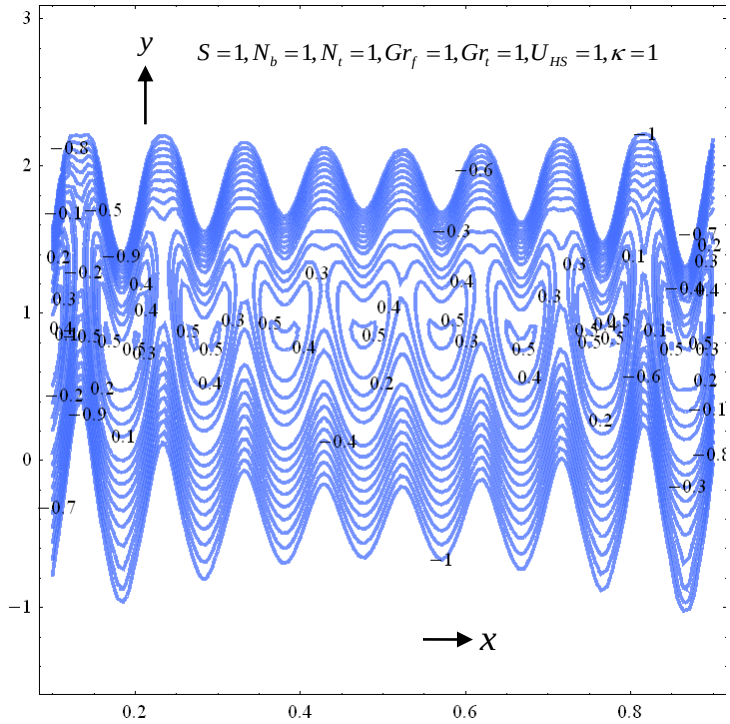
$S=1, N_b=1, N_t=1, Gr_f=1, Gr_t=1, U_{HS}=1, \kappa=1$
y
x

(c)

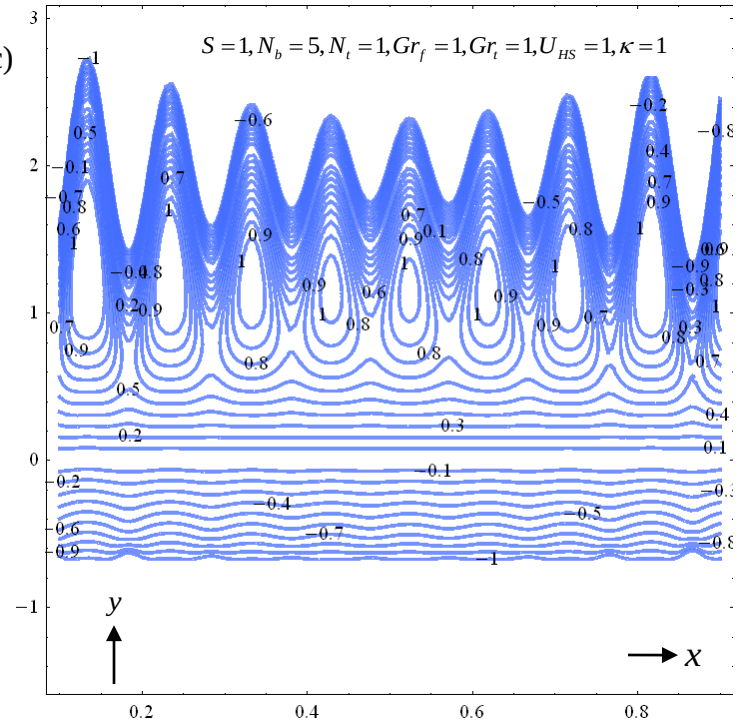
$S=1, N_b=5, N_t=1, Gr_f=1, Gr_t=1, U_{HS}=1, \kappa=1$
y
x

(d)

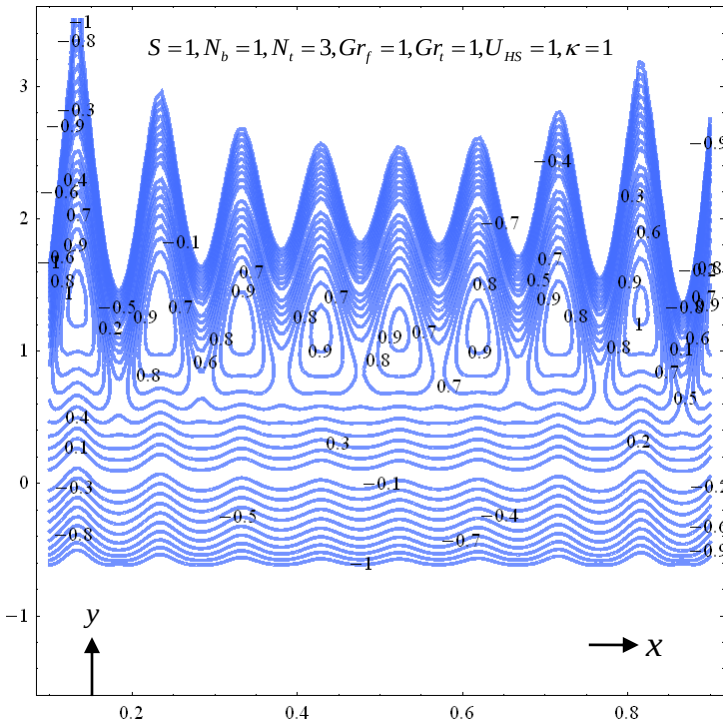
$S=1, N_b=1, N_t=3, Gr_f=1, Gr_t=1, U_{HS}=1, \kappa=1$
y
x

(e)

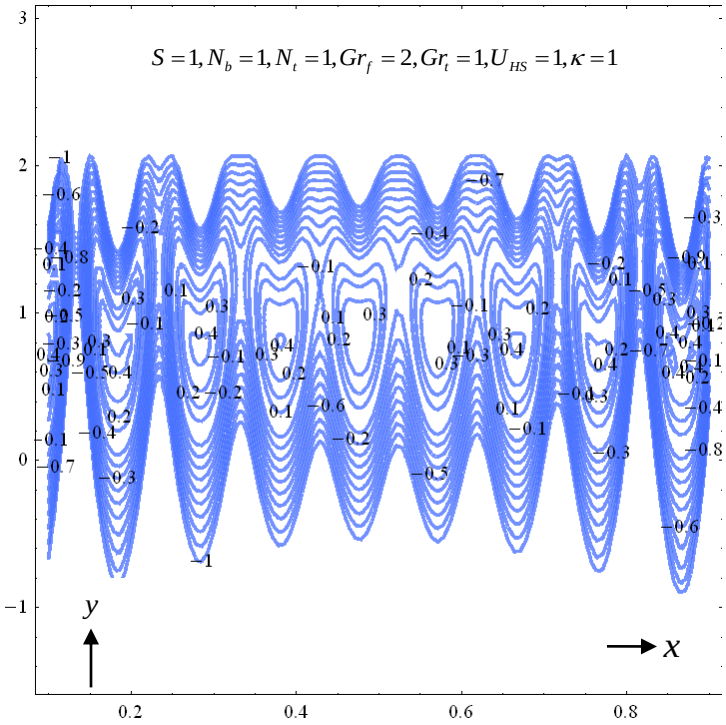
$S=1, N_b=1, N_t=1, Gr_f=2, Gr_t=1, U_{HS}=1, \kappa=1$
y
x

(f)

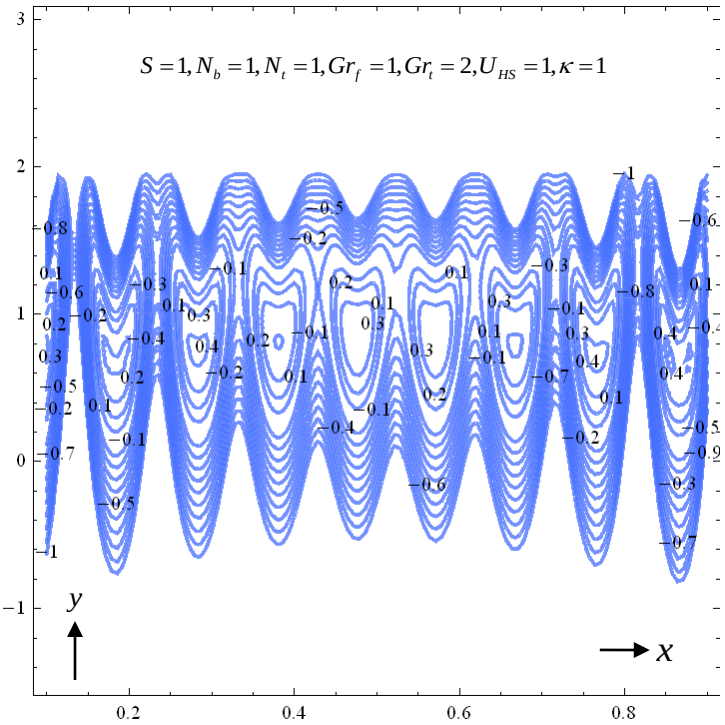
$S=1, N_b=1, N_t=1, Gr_f=1, Gr_t=2, U_{HS}=1, \kappa=1$
y
x

(g)

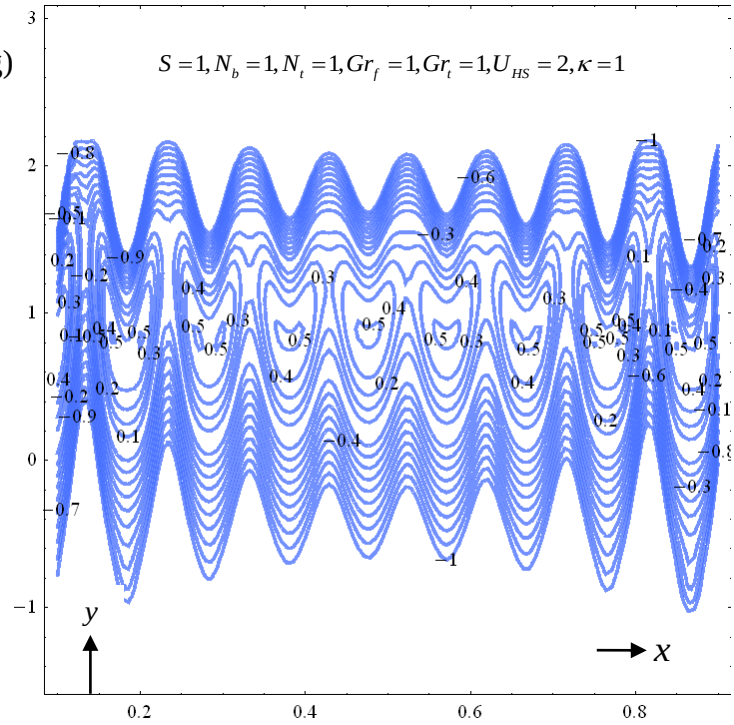

(h)

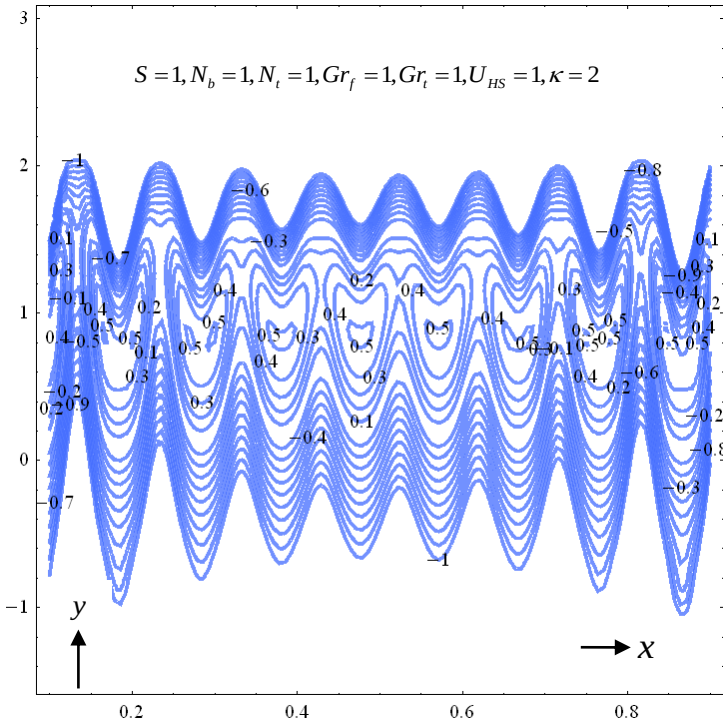

Fig.9 (a)-(g). Stream lines at $\bar{Q}=0.9$ for various parameters

A constant axial pressure gradient scenario is considered and a finite thickness of the Debye electrical double layer. Plots are visualized only for the upper channel half space ($0<y<h$) due to symmetrical boundary conditions.

Fig.2. depicts the response in temperature for different values of Joule heating parameter (S), across the upper micro-channel half space. An increase in positive values of S significantly elevates temperature. Negative values of S however generate the opposite effect and cool the nanofluid. In all cases there is a growth from the centerline ($y = 0$) to the upper micro-channel wall ($y = h$). The profiles evolve from approximately linear distribution for $S <0$ to a strongly parabolic profile for $S > 0$. $S = \sigma E_x^2 a^2 / k(T_1 - T_0)$. This parameter reflects that stronger axial electrical field (E_x) with all other parameters constrained, enhances the contribution of Joule heating. The effect appears in the energy (heat) conservation eqn. (8) as an isolated term, $+S$. The case of $S = 0$ (absence of Joule heating) as expected falls between the results for $S < 0$ and $S> 0$. The influence of Joule heating is also associated with the imposition of low Péclet number. This assists in reverse thermal diffusion of heat from the entry zone to the exit zone of the channel which will impact on temperature evolution across the semi-span of the micro-channel. The Joule resistive heating overall exerts a substantial effect on the thermal field in the micro-channel.

Fig. 3 depicts the response in nano-particle volume fraction (F) with Joule heating parameter (S). The opposite behavior is computed compared with temperature field. With positive value of *S, there is a strong depletion in* F values which are infact negative for considerable distance across the micro-channel from the centreline. Only at relatively high values of transverse coordinate (y), are positive F values achieved. With negative S value, there is a weak negativity inn profile near the centreline; however there is a strongly positive growth in nano-particle volume fraction across the majority of the upper micro-channel half-span. Imposition of stronger axial electrical field enhances Joule heating and the associated electric conduction and clearly modifies nano-particle distribution significantly throughout the upper micro-channel zone. With absence of Joule heating, there is still a negative trend in F values for much of the transverse coordinate value; however there is a positive growth commencing at greater values of y

and this trend is achieved earlier than for the case of positive S value. Effectively the presence of Joule heating influences markedly the diffusion of nano-particles in the regime.

Figs.4(a)-(g) present the evolution in axial velocity profile for different values of (a) Joule heating parameters (b) Brownian motion parameter (c) thermophoresis parameter (d) basic-density Grashof number (e) thermal Grashof number (f) Helmholtz-Smoluchowski velocity (g) Debye length. The axial pressure is fixed at unity in these plots. Fig. 4a clearly demonstrates that with negative Joule heating there is a significant deceleration whereas with positive Joule heating there is a marked acceleration. In all cases the distributions are semi-parabolic since the maximum velocity arises at the channel centre (only the upper channel half space is included). At the upper microchannel wall the no-slip boundary condition enforces a zero velocity (the same will be present at the lower microchannel wall, not shown). When electrical field (axial) is increased, the Joule parameter (for constant temperature difference) is also enhanced. This results in boosting the momentum for positive S value and decreasing momentum for negative S value. The absence of Joule heating falls between these two cases. Fig. 4b shows that an increase in Brownian motion parameter (N_b) induces strong acceleration in the axial flow. N_b in the Buongiorno formulation [11] is related to the size of spherical nano-particles. Larger values correspond to smaller nano-particle size which leads to axial acceleration. Smaller N_b values are associated with larger nano-particles manifesting in axial flow deceleration. The exact mechanism of Brownian motion in nanofluids is still a topic of some debate. It is however generally accepted that ballistic collisions are elevated with smaller nano-particles and that the Brownian motion forces are enhanced for smaller nano-particles which effectively boosts momentum development [44]. Fig. 4c indicates that with increasing thermophoresis parameter (N_t) there is a weak acceleration in the axial flow. This is amplified in the central zone of the channel. Greater thermophoresis implies stronger migration of nano-particles under a temperature gradient away from the micro-channel walls. This influences the thermal field and in turn modifies the velocity field, via coupling terms between the momentum equation and energy equations i.e. buoyancy terms. Fig. 4d demonstrates that with increasing basic-density (nano-particle solutal) Grashof number there is a tangible retardation induced in the axial flow. The

opposite effect is generated (i.e. acceleration) with an increase in thermal Grashof number as observed in Fig 4e. The buoyancy forces associated with solutal and thermal effects are therefore not consistent in their impact on the axial flow development. Furthermore a much stronger modification in axial velocity is caused with greater thermal Grashof number compared with a less prominent reduction in axial velocity with solutal Grashof number. With an absence of solutal buoyancy effect (Gr_f=0) the axial velocity is a maximum whereas with an absence of thermal buoyancy force (Gr_t = 0) the axial velocity is a minimum. In both figures 4d and 4e axial flow reversal (backflow) is never induced since positive values are sustained across the upper microchannel half space. Fig. 4f reveals that with an increase in U_{HS} i.e. the Helmholtz-Smoluchowski velocity (or maximum electro-osmotic velocity), from 0 (vanishing axial electrical field) to 1, there is initially a strong acceleration in the axial flow. However for U_{HS} =2 i.e. with subsequent increase in axial electrical field, there is a significant deceleration induced. A critical electrical field strength there exists beneath which the flow is assisted and above which it is impeded. A similar trend has been reported in Ranjit *et al*. [45]. In fig 4g it is evident that an increase in Debye–Hückel parameter (κ) substantially accelerates the axial flow. It also dramatically modifies the shape of the velocity profile, which evolves from a monotonic decay from the centre-line to the upper micro channel wall (for κ = 2) to a plateau profile for much of the micro-channel half space eventually descending sharply at the upper micro-channel wall for κ = 10 and 20. Although κ =does not appear explicitly in the conservation eqns. (6)-(9), it does feature in the term $\frac{\partial^2 \Phi}{\partial y^2} = \kappa^2 \Phi$ in the momentum eqn (7). Debye–Hückel parameter is the *reciprocal* of Debye length. Reducing Debye length i.e. increasing Debye–Hückel parameter is known [46, 47] to increase the electrical potential since enhanced migration of ions arises as we progress away from the charged surface (micro-channel walls). Debye length is therefore a critical design parameter in controlling the electrical potential distribution which in turn influences markedly the axial velocity field.

Figs.5 (a)-(g) present the variation in volumetric flow rate along the channel length i.e. with axial coordinate (x) for various parameter combinations. In all plots the *asymmetric* nature of the peristaltic wave propagation is clearly captured with significantly greater

amplitudes computed at the entry zone to the micro-channel (x~0). Amplitudes generally decrease with increasing axial distance but are increased again at the exit zone (x~1.0). Fig 5a shows that with positive Joule parameter ($S>0$), the amplitudes are boosted i.e. flow rate is accentuated throughout the extent of the micro-channel. The contrary behavior is computed with negative Joule parameter ($S<0$). Increasing Brownian motion parameter, N_b, also strongly enhances volumetric flow rate (fig. 5b) in particular at the entry zone of the micro-channel and to a lesser extent at the exit zone. A weak but non-trivial increase in flow rate is also induced with greater thermophoresis parameter (N_t), as shown in fig 5c. Again the effect is amplified at the entry and exit regions of the micro-channel and is stifled at intermediate axial distances. Increasing nano-particle (solutal) Grashof number, Gr_f is observed to strongly depress the magnitudes of volumetric flow rate (fig. 5d) whereas a slight enhancement in flow rates accompanies an increase in thermal Grashof number (Gr_t), as plotted in fig. 5e. Solutal buoyancy effects therefore impact more significantly on flow rates than thermal buoyancy effects. With increasing positive U_{HS} i.e. the Helmholtz-Smoluchowski velocity, flow rates are markedly increased whereas they are strongly reduced with negative U_{HS}. Again the asymmetry in distributions is clearly computed in fig. 5f owing to the imposition of different peristaltic wave forms at the upper and lower walls of the mciro-channel. We further note that both vanishing (U_{HS}= 0) and negative U_{HS} result in negative flow rates i.e. backflow in the micro-channel. This is only eliminated for the case of positive Helmholtz-Smoluchowski velocity. Fig 5g indicates that with greater values of Debye–Hückel parameter (κ) i.e. lower values of the Debye electro-osmotic length, there is initially a considerable elevation in the volumetric flow rate, Q. However when the Debye–Hückel parameter (κ) is doubled from 10 to 20 the subsequent increment in flow rates is marginal indicating that flow rates are optimized at lower values than 20. In all cases Q characteristics remain positive i.e. backflow is not induced anywhere along the micro channel for any value of Debye–Hückel parameter (κ).

Figs. 6(a)-(g) illustrate the distribution of pressure difference across one wavelength (Δp) with time averaged volumetric flow rate ($\overline{Q}$) for selected nanoscale and electro-osmotic parameters. Three pumping regimes are of importance, namely the *pumping region* ($\Delta p >$ 0), the *augmented pumping region* ($\Delta p <$ 0), and the *free pumping region* (Δp =0).

Generally, in the pumping region, pressure difference increases with negative flow rates whereas it is reduced with positive flow rates. The Δp-$\overline{Q}$ relationship is clearly an inverse linear relationship i.e. pressure difference decreases with increasing time averaged flow rate. Fig 6a shows that for negative Joule heating (S) pressure difference is depressed for all values of time-averaged flow rate. However for positive values of Joule heating parameter, pressure difference is enhanced markedly over the entire range of values of $\overline{Q}$. A weak enhancement in pressure difference is induced with increasing Brownian motion parameter, N_b as seen in fig 6b, whereas they are more considerably elevated with increasing thermophoresis parameter (N_t), as plotted in fig. 6c. Negative pressure difference is computed only at very high values of time-averaged flow rate. Increasing nano-particle (solutal) Grashof number, Gr_f very weakly elevates the pressure difference (fig. 6e) whereas a more significant increase is caused by increasing thermal Grashof number (Gr_t), as shown in fig. 6e. Pressure difference is also boosted with positive Helmholtz-Smoluchowski velocity (U_{HS}) whereas it is decreased with negative Helmholtz-Smoluchowski velocity, as depicted in fig. 6f. Finally an increase in Debye–Hückel parameter (κ), as illustrated in fig. 6g, from 2 to 10, induces initially a considerable elevation in the pressure difference, whereas with subsequent increase in κ to 20, results in a relatively weak enhancement.

Figs. 7 (a)-(g) present the response in skin friction i.e. wall shear stress function (C_f) along the channel length with selected parameters. Maximum shear stress arises at the fully contracted walls of the micro-channel and the minimum is associated with fully relaxed walls. Maximum impedance is generated to the peristaltic flow at the fully contracted walls and the opposite behavior arises when the walls are fully relaxed. The constriction in the walls when fully contracted serves to oppose the flow and manifests in an elevation in frictional resistance at the walls i.e. greater wall shear stress (skin friction). As with velocity plots described earlier, the maximum amplitudes of shear stress correspond to the entry zone of the micro-channel and high values are also computed at the exit zone. At intermediate locations there is a depression in the amplitudes. With positive Joule parameter ($S>0$), fig 7a shows that the skin friction amplitudes are consistently increased along the micro-channel length whereas they are reduced with negative Joule parameter ($S<0$). Increasing Brownian motion parameter, N_b

(fig 7b) and increasing thermophoresis parameter, N_t (fig 7c) both induce a weak increase in skin friction amplitudes. Greater nano-particle (solutal) Grashof number, Gr_f (fig. 7d) suppresses skin friction whereas increasing thermal Grashof number (Gr_t) elevates skin friction values. The cases of Gr_f =0 and Gr_t =0 correspond to vanishing nano-solutal and thermal buoyancy and result in maximum and minimum skin friction values in figs. 7d and 7e respectively. With positive U_{HS} value (fig. 7f), there is an increase in skin friction. Negative Helmholtz-Smoluchowski (U_{HS} < 0) velocity also increases skin friction and results in higher magnitudes. The peaks and troughs for these two cases appear in an alternating fashion across the micro-channel length. With vanishing Helmholtz-Smoluchowski velocity (U_{HS} = 0) skin friction magnitudes are significantly suppressed with a small peak only arising near the entry zone of the micro-channel. With increasing Debye–Hückel parameter (κ) (decreasing Debye electro-osmotic length), skin friction is greatly enhanced throughout the micro-channel length, as shown in fig. 7g.

Fig.8. illustrate the evolution in wall heat transfer rate (Nusselt number) along the micro-channel length with respective variations in (a) Joule heating parameter (b) Brownian motion parameter (c) thermophoresis parameter. A significant enhancement in Nusselt number is generated with a negative Joule dissipation parameter value (S <0) whereas a reduction is caused with positive Joule dissipation parameter value (S >0), as observed in fig. 8a. The reduction in temperatures associated with negative Joule dissipation parameter value (S <0) results in a *net migration of heat away from the nanofluid towards the micro-channel walls* (nanofluid cooling and wall heating) and the opposite behaviour (nanofluid heating and wall cooling) is associated with positive Joule dissipation parameter value (S >0). With increasing Brownian motion parameter (N_b), as seen in fig. 8b, and also increasing thermophoresis parameter (N_t) as depicted in fig. 8c, there is a noticeable decrease in Nusselt numbers at all values of axial coordinate. The thermal enhancement in the nanofluid (increased temperatures) draws thermal energy away from the micro-channel walls. The nanoscale parameters therefore both induce cooling at the micro-channel walls.

Figs 9a-g present the streamline distributions for various combinations of the key electro-osmotic, nanofluid and buoyancy parameters. The benchmark case is fig 9b where all parameters are prescribed unity values. Each of the other figures is compared respectively

with this case to elucidate the influence of the respective parameter being varied on the growth of trapped zones. These figures visualize a key characteristic of peristaltic flows, namely trapping phenomenon which relates to the stream lines circulation and formation of a trapped bolus. It allows the determination of reflux characteristics and also vortex growth and circulation intensity in peristaltic flows. In all the plots there is a significant lack of symmetry about the centre line (y =0) owing to the dissimilar peristaltic wave prescribed at the lower and upper micro-channel. Considering fig 9a (S=-1) relative to fig 9b (S=+1) with all other parameters fixed at unity, it is evident that the peristaltic flow is intensified in the central zone as testified to by the emergence of multiple vortex zones around the micro-channel centerline. Streamline concentration is much weaker in the lower micro-channel half-space in fig 9a compared with fig. 9b. The nature of the Joule heating (dissipation) considerably influences the structure of the flow. Fig 9c (N_b=5) illustrates the streamline distribution with a much greater Brownian motion parameter effect compared with fig 9b (N_b =1). The shield-shaped dual trapped zones in the upper half space are transformed into tear-drop shaped single boluses with increasing N_b nd the distorted streamlines in the lower zone are almost completely eliminated with streamlines aligning more evenly for higher Brownian motion parameter. There is also significant damping of the flow around the centerline. Fig. 9d illustrates the influence of greater thermophoresis parameter (Nt) which is increased to 3 compared with unity value in fig. 9a. There is substantial modification in the vortex zones in the upper section of the channel with stronger thermophoretic body force; they become singular in nature and are widened towards the centre-line, forming more triangular patterns. Simultaneously the significant streamline distortion in the lower channel periphery vanishes with increasing thermophoresis although there is some distortion in the streamlines along the core region of the micro-channel. Increasing solutal Grashof number (Gr_f) to 2 (fig. 9e) weakly modifies the streamline patterns compared with fig 9b (Gr_f =1). The shield-shaped zones grow at the centre whereas they are squashed at the upper section and stretched at the lower section of the micro-channel. Doubling the solutal (nano-particle species) buoyancy force therefore does impact on trapping phenomena in the regime. The modification induced with increasing thermal Grashof number (Gr_t =2 in fig 9f compared with Gr_t = 1 in fig 9b) is similar to that caused with increasing solutal buoyancy force,

but less stretching downwards of the lower zone streamline patterns is caused. Increasing Helmholtz-Smoluchowski velocity (U_{HS}) and Debye–Hückel parameter (κ) (decreasing Debye electro-osmotic length), as presented in fig 9g and 9h, respectively, both result in a slight compression of the central vortex zones i.e. boluses, compared with the benchmark case, fig. 9b.

4. CONCLUSIONS

Motivated by new developments in ocular pharmacological delivery systems, a mathematical model has been developed for peristaltic electro-osmotic nanofluid flow in a micro-channel with different wave forms imposed at the walls. Joule heating and thermal and species (solutal) buoyancy effects have been included. The non-dimensional boundary value problem has been solved with integration methods subject to isothermal boundary conditions at the walls. The key parameters dictating the thermal and hydrodynamic behavior have been shown to be the thermal and solutal (basic density) Grashof numbers, nanoscale Brownian motion parameter, thermophoresis parameter, Helmholtz-Smoluchowski velocity (maximum electro-osmotic velocity), Debye electrokinetic length and Joule heating to surface heat flux ratio. Mathematica software has been implemented to numerically evaluate the effects of these parameters on nano-particle volume fraction, temperature, axial velocity, averaged volumetric flow rate, pressure difference across one wavelength, skin friction (wall shear stress function), Nusselt number (wall heat transfer rate) and stream function distribution in the wave frame. The computations have shown that:

- Increasing Brownian motion parameter strongly accelerates the axial flow and strongly increases volumetric flow rate whereas it weakly increases pressure difference and skin friction. However it reduces the Nusselt number and eliminates distortion in streamlines in the lower micro-channel half space.
- Increasing thermophoresis parameter weakly accelerates the axial flow, weakly increases Nusselt number and slightly enhances volumetric flow rate whereas it strongly increases pressure difference along the channel and results in the growth of triangular boluses in the central zone.

- Increasing positive Joule parameter significantly increases nanofluid temperature, reduces nano-particle volume fraction (concentration), accelerates the axial flow, boosts the volumetric flow rate, increases pressure difference and skin friction, decreases Nusselt number and generates stronger bolus formation in the central zone. Negative Joule parameter induces the opposite effects and results in stronger boluses in the upper zone of the micro-channel.
- Increasing nano-particle solutal Grashof number decelerates the axial flow, decreases volumetric flow rate, weakly increases pressure difference, reduces skin friction, and results in stronger and narrower boluses in the central zone of the micro-channel.
- Increasing thermal Grashof number accelerates the axial flow significantly, weakly increases volumetric flow rate, markedly increases the pressure difference, substantially elevates skin friction at the walls, and also generates stronger and narrower boluses in the core zone of the micro-channel.
- Increasing positive Helmholtz-Smoluchowski velocity accelerates the axial flow, enhances the volumetric flow rate, increases pressure difference, increases skin friction and leads to a weak compression in streamlines in the upper zone peripheral area. Negative Helmholtz-Smoluchowski velocity generally induces the contrary effects except that it also leads to an increase in skin friction but with lower magnitudes than those computed with positive Helmholtz-Smoluchowski velocity.
- Increasing Debye–Hückel parameter (κ) (decreasing Debye electro-osmotic length) considerably accelerates the axial flow, enhances volumetric flow rate, increases pressure difference and skin friction and slightly compresses the streamline patterns.

The current results are relevant to elucidating fluid dynamics of proposed novel drug delivery systems. However they have neglected both *slip effects* at the walls of the micro-channel and also *non-Newtonian properties* of the electrolytic nanofluid. Furthermore entropy generation minimization is also an important aspect of optimizing nano-electro-osmotic pumping designs in pharmacology [X]. All these areas will therefore be addressed in the future.

REFERENCES

1. Mikityuk M.V.: Nanoparticles and prospects for their application in biology and medicine. *Problems Ecology Med*., 15(5-6): 42-50 (2011).
2. P. Muthuraman, K. Ramkumar and D.H. Kim: Analysis of dose-dependent effect of zinc oxide nanoparticles on the oxidative stress and antioxidant enzyme activity in adipocytes *Appl. Biochem. Biotechnol.*, 174: 2851–2863 (2014).
3. D. Archana. Brijesh K. Singh. Joydeep Dutta. P.K. Dutta, Chitosan-PVP-nano silver oxide wound dressing: *In vitro* and *in vivo* evaluation, *Int. J. Biological Macromolecules*, 73, 49-57 (2015).
4. Y. Qazi, B. Stagg, B. Ambati, Nanoparticles in ophthalmic medicine. *International Journal of Green Nanotechnology: Biomedicine*, 1, 10-24 (2009).
5. Seyfoddin, A., Shaw, J., Al-Kassas, R. (2010). Solid lipid nanoparticles for ocular drug delivery. *Drug Delivery, 17*, 1–23.
6. Kambhampati, S. P., & Kannan, R. M. (2013). Dendrimer nanoparticles for ocular drug delivery, *J. Ocular Pharmacology and Therapeutics, 29*(2), 151–165.
7. A. Sohail et al, A review on hyperthermia via nanoparticle-mediated therapy, Bulletin du Cancer. http://doi.org/10.1016/j.bulcan.2017.02.003,
8. Q. Wu, Haiyan Zhang, Minshan Chen,Yaojun Zhang, Junting Huang, Zuowen Xu, Wenguang Wang, Preparation of carbon-coated iron nanofluid and its application in radiofrequency ablation, *J. Biomedical Materials Research- Part B: Applied Biomaterials*, 103, 908–914 (2015).
9. A. Pendleton; Prasenjit Kar; Subrata Kundu; Sahar Houssamy; Hong Liang, Effects of nanostructured additives on boundary lubrication for potential artificial joint applications, *ASME J. Tribol.*, 132, 031201-031201-5 (2010).
10. S. Choi, Enhancing thermal conductivity of fluids with nanoparticles. In: *Siginer DA, Wang HP (eds) Developments and applications of non-Newtonian flows, FED, vol 231/MD, vol 66. ASME, New York*, pp 99–103 (1995).
11. J. Buongiorno, Convective transport in nanofluids, *ASME J. Heat Transfer*, 128(3) 240-250 (2006).

12. R.K. Tiwari, M.K. Das, Heat transfer augmentation in a two-sided lid-driven differentially heated square cavity utilizing nanofluids, *Int. J. Heat Mass Transfer*, 50, 2002–2018 (2007).
13. Nur Amalina Abdul Latiff, Md Jashim Uddin, O Anwar Bég, Ahmad Izani Ismail, Unsteady forced bioconvection slip flow of a micropolar nanofluid from a stretching/shrinking sheet, *Proceedings of the Institution of Mechanical Engineers, Part N: Journal of Nanomaterials, Nanoengineering and Nanosystems*, 230, 177-187 (2016).
14. Tan, J., Thomas, A. & Liu, Y. Influence of red blood cells on nanoparticle targeted delivery in microcirculation. *Soft Matter*, 8, 1934-1946 (2012).
15. F. Gentile, M. Ferrari, P. Decuzzi, The transport of nanoparticles in blood vessels: the effect of vessel permeability and blood rheology, *Ann. Biomed Eng*., 36 (2): 254-61 (2008).
16. O. Anwar Bég, M. Faisal Md Basir, M.J. Uddin, and A. I. Md. Ismail, Numerical study of slip effects on asymmetric bioconvective nanofluid flow in a porous microchannel with an expanding/contracting upper wall using Buongiorno's model, *J. Mechanics in Medicine and Biology*, 17 (5) 1750059 (28 pages) (2017). DOI: 10.1142/S0219519417500592.
17. J. Tan, S. Wang, J. Yang and Y. Liu, Coupled particulate and continuum model for nanoparticle targeted delivery. *Comput. Struct. 122*, 128–134 (2013).
18. O. Anwar Bég, M.M. Rashidi, M. Akbari, A. Hosseini, Comparative numerical study of single-phase and two-phase models for bio-nanofluid transport phenomena, *J. Mechanics in Medicine and Biology*, 14, 1450011.1-31 (2014).
19. J. Tan, W. Keller, S. Sohrabi, J. Yang and Y. Liu, Characterization of nanoparticle dispersion in red blood cell suspension by the lattice Boltzmann-immersed boundary method, *Nanomaterials*, 6, 30; 1-14 (2016).
20. M. Jaffrin and H. Shapiro, Peristaltic pumping, *Annual Review of Fluid Mechanics*, 3(1): 13-37 (1971).
21. L. von Segesser, A. Jeanjacquot, P. Meyer, J.B. Buchs, Arthropump with peristaltic effect and pulsatile flow, *J. Biomedical Engineering*, 6, 146-150 (1984).

22. L.-S.Jang, Y.-J.Li, S.-J.Lin, Y.-C.Hsu, W.-S.Yao, M.-C. Tsai, C.-C. Hou, A stand-alone peristaltic micropump based on piezoelectric actuation, *Biomed. Microdev*., 9, 185–194 (2007).
23. C. de Loubens *et al*., A lubrication analysis of pharyngeal peristalsis: application to flavour release, *J. Theoretical Biology*, 267, 300-311 (2010).
24. J. Hœpffner and K. Fukagata, Pumping or drag reduction? *J. Fluid Mechanics*, 635, 171-187 (2009).
25. M. S. Longuet-Higgins, Peristaltic pumping in water waves, *J. Fluid Mechanics*, 137, 393-407 (1983).
26. D.E. Wilson and R.L. Panton, Peristaltic transport due to finite amplitude bending and contraction waves, *J. Fluid Mechanics*, 90, 145-159 (1979).
27. B.B. Gupta, V. Seshadri, Peristaltic pumping in non-uniform tubes, *J. Biomechanics*, 9, 105–109 (1976).
28. T. Ishikawa, T. Sato, G. Mohit, Y. Imai, T. Yamaguchi, Transport phenomena of microbial flora in the small intestine with peristalsis, *J. Theoretical Biology*, 279, 63-73 (2011).
29. O. Anwar Bég and D. Tripathi Mathematica simulation of peristaltic pumping with double-diffusive convection in nanofluids: a bio-nano-engineering model, *Proc. IMECHE Part N: J. Nanoengineering and Nanosystems* 225, 99–114 (2012).
30. N.S. Akbar, D. Tripathi and O. Anwar Bég, Modeling nanoparticle geometry effects on peristaltic pumping of medical magnetohydrodynamic nanofluids with heat transfer, *J. Mechanics in Medicine and Biology*, 16 (06), 1650088 (2016).
31. A. Babaie, M. H. Saidi and A. Sadeghi, Heat transfer characteristics of mixed electroosmotic and pressure driven flow of power-law fluids in a slit microchannel, *Int. J. Thermal Sciences*, 53, 71-79 (2012).
32. Y. Hu *et al.,* Electroosmotic flow in microchannels with prismatic elements, *Microfluidics and Nanofluidics*, 3, 151-160 (2007).
33. K. Masilamani, Suvankar Ganguly, Christian Feichtinger and Ulrich Rüde, Hybrid lattice-Boltzmann and finite-difference simulation of electroosmotic flow in a microchannel, *Fluid Dynamics Research*, 43, 025501 (2011).

34. M. Sadeghi, Arman Sadeghi and Mohammad Hassan Saidi, Electroosmotic flow in hydrophobic microchannels of general cross section, *ASME J. Fluids Eng.*, 138(3), 031104 (2015).
35. Q. Liao, T.Y. Wen, X. Zhu, Numerical investigations of electro-osmotic flows in triangle microchannels, *Applied Thermal Engineering*, 28, 1463–1470 (2008).
36. Marcos, K.T. Ooi, C. Yang, J.C. Chai, T.N. Wong, Developing electro-osmotic flow in closed-end micro-channels, *Int. J. Engineering Science*, 43, 1349–1362 (2005).
37. M.A. Bosse and P. Arce, Role of Joule heating in dispersive mixing effects in electrophoretic cells: convective-diffusive transport aspects, *Electrophoresis*, 21(5):1026-33 (2000).
38. X. Xuan and D. Li, Analytical study of Joule heating effects on electrokinetic transportation in capillary electrophoresis, *J. Chromatogr A.*, 1064(2):227-37 (2005).
39. D. Jing, Y. Pan, X. Wang, Joule heating, viscous dissipation and convective heat transfer of pressure-driven flow in a microchannel with surface charge-dependent slip, *Int. J. Heat Mass Transfer*, 108, 1305-1313 (2017).
40. H. Yavari, A. Sadeghi, M.H. Saidi, S. Chakraborty, Combined influences of viscous dissipation, non-uniform Joule heating and variable thermophysical properties on convective heat transfer in microtubes, Int. J. Heat Mass Transfer, 55, 762–772 (2012).
41. A. Sutradhar, J. K. Mondal, P. V. S. N. Murthy and Rama Subba Reddy Gorla, Influence of Starling's hypothesis and Joule heating on peristaltic flow of an electrically conducting Casson fluid in a permeable microvessel, *ASME J. Fluids Eng* 138(11), 111106 (2016).
42. T. Hayat, Shafique M, Tanveer A, Alsaedi A, Radiative peristaltic flow of Jeffrey nanofluid with slip conditions and Joule heating. *PLoS ONE* 11(2): e0148002 (2016). doi:10.1371/journal.pone.0148002.
43. D. Tripathi, Ashish Sharma and O. Anwar Bég, Electrothermal transport of nanofluids via peristaltic pumping in a finite micro-channel: *effects of Joule*

heating and Helmholtz-Smoluchowski velocity, Int. J. Heat Mass Transfer, 111, 138–149 (2017).

44. W.E. Evans, J. Fish and P. Keblinski, Role of Brownian motion hydrodynamics on nanofluid thermal conductivity, *Appl. Phys. Lett.* 88, 093116 (2006).
45. N.K. Ranjit, G.C. Shit' , A. Sinha, Transportation of ionic liquids in a porous micro-channel induced by peristaltic wave with Joule heating and wall-slip conditions, *Chemical Engineering Science* (2017). https://doi.org/10.1016/j.ces.2017.06.012
46. D.A. Saville, Electrokinetic effects with small particles, *Ann. Rev. Fluid Mechanics*, 9, 321-337 (1977).
47. G. D. Ngoma and F. Erchiqui, Pressure gradient and electroosmotic effects on two immiscible fluids in a microchannel between two parallel plates, *J. Micromech. Microeng.*, 16, 83-90 (2005).
48. M. M. Bhatti, M. Sheikholeslami and A. Zeeshan, Entropy Analysis on Electro-Kinetically Modulated Peristaltic Propulsion of Magnetized Nanofluid Flow through a Microchannel,. *Entropy,* 19(9), 481 (2017)

APPENDIX

The electric potential within the microchannel is given by the well-known Poisson-Boltzmann equation:

$$\nabla^2\bar{\Phi} = -\frac{\bar{\rho}_e}{\varepsilon}, \qquad \text{(A1)}$$

where $\bar{\rho}_e = ez(\bar{n}^+ - \bar{n}^-)$ is the electrical charge density, $\bar{n}_+$ and $\bar{n}_-$ are positive and negative ions having bulk concentration (number density) n_0 and a valence of z_+ and z_- respectively, and e represents elementary charge.

The Nernst-Planck equation is defined to determine the potential distribution and describe the charge number density as:

$$\frac{\partial \bar{n}_{\pm}}{\partial \bar{t}} + (\mathbf{q}.\nabla)\bar{n}_{\pm} = D\nabla^2 \bar{n}_{\pm} \pm \frac{Dze}{k_B T}\left(\nabla.\left(\bar{n}_{\pm}\nabla\bar{\Phi}\right)\right), \tag{A2}$$

where D represents the diffusivity of the chemical species. After non-dimensionalization of Eq.(A2), the *nonlinear terms* appear to the $O\left(Pe\,\delta^2\right)$, where $Pe = Re\,Sc$ represents the ionic Peclét number and $Sc = \mu/\rho_f D$ denotes the Schmidt number. Using the limitations *Re, Pe,* $\delta << 1$, the Poisson equation is obtained as:

$$\frac{\partial^2 \Phi}{\partial y^2} = -\kappa^2\left(\frac{n_+ - n_-}{2}\right), \tag{A3}$$

The Nernst-Planck equation is simplified to:

$$0 = \frac{\partial^2 n_{\pm}}{\partial y^2} \pm \frac{\partial}{\partial y}\left(n_{\pm}\frac{\partial \Phi}{\partial y}\right), \tag{A4}$$

subject to boundary conditions $n_{\pm} = 1$ at $\Phi = 0$ and $\partial n_{\pm}/\partial y = 0$ where $\partial\Phi/\partial y = 0$ (bulk conditions). These yield:

$$n_{\pm} = e^{\mp\Phi}. \tag{A5}$$

Using equations (A3) and (A5), the Poisson-Boltzmann paradigm is obtained as:

$$\frac{\partial^2 \Phi}{\partial y^2} = \kappa^2 \sinh\left(\Phi\right). \tag{A6}$$

The values of A_{11}, A_{12}, A_{13}, A_{14} used in Eq.(14) are given as:

$$A_{11} = 6h^3(Gr_t N_b + Gr_f N_t)(N_b + N_t + h^2 S), \tag{A7}$$

$$\begin{aligned} A_{12} = {} & (3hN_b(N_b+N_t)^3(h^2\frac{\partial p}{\partial x} - 2U_{HS} - \frac{\partial p}{\partial x}y^2) + Gr_t h^2 N_b(-6h(N_b+N_t) \\ & + h^3(-6 + N_b{}^2 + 2N_b N_t + N_t{}^2)S - (N_b+N_t)^2 Sy^3) + Gr_f(h^3(N_b{}^4 \\ & - 6N_b N_t + 4N_b{}^3 N_t - 6N_t{}^2 + 6N_b{}^2 N_t{}^2 + 4N_b N_t{}^3 + N_t{}^4) \\ & + h^5 N_t(-6 + N_b{}^2 + 2N_b N_t + N_t{}^2)S - (N_b+N_t)^4 \mathrm{y}^3 - h^2 N_t(N_b+N_t)^2 Sy^3)), \end{aligned} \tag{A8}$$

$$
\begin{aligned}
A_{13} = {} & (N_b + N_t)(-3hN_b(N_b + N_t)^2(h^2\frac{\partial p}{\partial x} - 2U_{HS} - \frac{\partial p}{\partial x}y^2) \\
& + Gr_t hN_b(h-y)(2h^3(-3+N_b+N_t)S + 3(N_b+N_t)^2 y + 2h^2(N_b+N_t)Sy \\
& + h(N_b+N_t)(-6+3N_b+3N_t-Sy^2)) + Gr_f(h-y)(2h^4N_t(-3+N_b+N_t)S \\
& - h(N_b-2N_t)(N_b+N_t)^2 y + 2h^3N_t(N_b+N_t)Sy \\
& - (N_b+N_t)^3 y^2 - h^2(N_b+N_t)({N_b}^2 - N_bN_t + N_t(6-2N_t+Sy^2)))),
\end{aligned}
\tag{A9}
$$

$$
A_{14} = -6(-1+e^{N_b+N_t})hN_b(N_b+N_t)^3 U_{HS}\cosh(y\kappa)\operatorname{sech}(y\kappa)). \tag{A10}
$$

The volumetric flow rate is derived as:

$$
\begin{aligned}
Q = {} & (-6h^4(Gr_tN_b + Gr_fN_t)(N_b+N_t+h^2S)/(N_b+N_t) + 6e^{N_b+N_t}h^4(Gr_tN_b+Gr_fN_t)(N_b+N_t+h^2S)/(N_b+N_t) \\
& + 3e^{N_b+N_t}h^4(N_b+N_t)(Gr_tN_b+Gr_fN_t)(N_b+N_t+h^2S) \\
& + \frac{1}{4}(-1+e^{N_b+N_t})h^4(N_b+N_t)^2(Gr_th^2N_bS + Gr_f({N_b}^2 + 2N_bN_t + N_t(N_t+h^2S))) \\
& - h^4(N_b+N_t)^2(N_b(N_b+N_t)\frac{\partial p}{\partial x} + e^{N_b+N_t}(-N_b(N_b+N_t)\frac{\partial p}{\partial x} + Gr_tN_b(N_b+N_t+h^2S) \\
& + Gr_fN_t(N_b+N_t+h^2S))) + h^2(Gr_fh^2(-(-1+e^{N_b+N_t}){N_b}^4 - (-4+e^{N_b+N_t}){N_b}^3N_t \\
& + N_t(-6+2e^{N_b+N_t}(-3+N_t)N_t + {N_t}^2)(N_t+h^2S) + {N_b}^2N_t(6N_t+h^2S+e^{N_b+N_t}(-6+3N_t+2h^2S)) \\
& + N_bN_t(-6+4{N_t}^2+2h^2N_tS + e^{N_b+N_t}(5{N_t}^2 - 6h^2S + 4N_t(-3+h^2S)))) + Gr_th^2N_b(3e^{N_b+N_t}{N_b}^3 + 3e^{N_b+N_t}{N_t}^3 \\
& - 6h^2S - 6N_t(1+e^{N_b+N_t}h^2S) + {N_t}^2(h^2S + 2e^{N_b+N_t}(-3+h^2S)) + {N_b}^2(h^2S + e^{N_b+N_t}(-6+9N_t+2h^2S)) + N_b(-6 \\
& + 2h^2N_tS + e^{N_b+N_t}(9{N_t}^2 - 6h^2S + 4N_t(-3+h^2S)))) - 3(-1+e^{N_b+N_t})N_b(N_b+N_t)^3(h^2\frac{\partial p}{\partial x} - 2U_{HS})) \\
& - 3(-1+e^{N_b+N_t})hN_b(N_b+N_t)^3U_{HS}(-1+\tanh(h\kappa))/\kappa \\
& - 3(-1+e^{N_b+N_t})hN_b(N_b+N_t)^3U_{HS}(1+\tanh(h\kappa))/\kappa)\big/(6(-1+e^{N_b+N_t})hN_b(N_b+N_t)^3).
\end{aligned}
\tag{A11}
$$

The axial pressure gradient is derived as:

$$
\begin{aligned}
\frac{\partial p}{\partial x} = {} & -\frac{1}{8h^3}(24Q + \frac{4e^{N_b+N_t}Gr_th^3(N_b+N_t+h^2S)}{(-1+e^{N_b+N_t})(N_b+N_t)} + \frac{4e^{N_b+N_t}Gr_fh^3N_t(N_b+N_t+h^2S)}{(-1+e^{N_b+N_t})N_b(N_b+N_t)} \\
& + \frac{24h^3(Gr_tN_b+Gr_fN_t)(N_b+N_t+h^2S)}{(-1+e^{N_b+N_t})N_b(N_b+N_t)^4} - \frac{24e^{Nb+Nt}h^3(Gr_tN_b+Gr_fN_t)(N_b+N_t+h^2S)}{(-1+e^{N_b+N_t})N_b(N_b+N_t)^4} \\
& - \frac{12e^{N_b+N_t}h^3(Gr_tN_b+Gr_fN_t)(N_b+N_t+h^2S)}{(-1+e^{N_b+N_t})N_b(N_b+N_t)^2} - \frac{h^3(Gr_th^2N_bS + Gr_f({N_b}^2+2N_bN_t+N_t(N_t+h^2S)))}{N_b(N_b+N_t)} \\
& - (4Gr_fh^3(-(-1+e^{N_b+N_t}){N_b}^4 - (-4+e^{N_b+N_t}){N_b}^3N_t + N_t(-6+2e^{N_b+N_t}(-3+N_t)N_t + {N_t}^2)(N_t+h^2S) \\
& + {N_b}^2N_t(6N_t+h^2S+e^{N_b+N_t}(-6+3N_t+2h^2S)) + N_bN_t(-6+4{N_t}^2+2h^2N_tS \\
& + e^{N_b+N_t}(5{N_t}^2 - 6h^2S + 4N_t(-3+h^2S)))))\big/((-1+e^{N_b+N_t})N_b(N_b+N_t)^3) \\
& - (4Gr_th^3(3e^{N_b+N_t}{N_b}^3 + 3e^{N_b+N_t}{N_t}^3 - 6h^2S - 6N_t(1+e^{N_b+N_t}h^2S) + {N_t}^2(h^2S + 2e^{N_b+N_t}(-3+h^2S)) \\
& + {N_b}^2(h^2S + e^{N_b+N_t}(-6+9N_t+2h^2S)) + b(-6+2h^2N_tS + e^{N_b+N_t}(9{N_t}^2 - 6h^2S + 4N_t(-3+h^2S))))) \\
& /(-1+e^{N_b+N_t})(N_b+N_t)^3 - 24hU_{HS} + 12U_{HS}\tanh(h\kappa)/\kappa).
\end{aligned}
\tag{A12}
$$

The stream function is derived as:

$$\psi = -(e^{-\frac{(N_b+N_t)y}{h}}(\cosh(h\kappa)+\sinh(h\kappa))((48e^{N_b+N_t}h^6(Gr_tN_b+Gr_fN_t)(N_b+N_t+h^2S)$$
$$+e^{\frac{(N_b+N_t)y}{h}}y(-24N_b(N_b+N_t)^4(-3h^2Q+h^3U_{HS}+Qy^2-hU_{HS}y^2)+Gr_th^3N_b(h^4(-72+N_b{}^3-24N_t$$
$$+3N_b{}^2N_t+N_t{}^3+3N_b(-8+N_t{}^2))S+24(N_b+N_b{}^2+N_t+2N_bN_t+N_t{}^2)y^2+2h(N_b+N_t)^3Sy^3$$
$$-3h^2(24N_t+8N_t{}^2-8Sy^2+N_b{}^3Sy^2-8N_tSy^2+N_t{}^3Sy^2+N_b{}^2(8+3N_tSy^2)+N_b(24+16N_t-8Sy^2$$
$$+3N_t{}^2Sy^2)))+Gr_fh^2(h^5N_t(-72+N_b{}^3-24N_t+3N_b{}^2N_t+N_t{}^3+3N_b(-8+N_t{}^2))S-3h(N_b{}^5+5N_b{}^4N_t$$
$$+10N_b{}^3N_t{}^2+2N_b{}^2N_t(-4+5N_t{}^2)+N_t{}^2(-8-8N_t+N_t{}^3)+N_bN_t(-8-16N_t+5N_t{}^3))y^2$$
$$+2(N_b+N_t)^5y^3+2h^2N_t(N_b+N_t)^3Sy^3+h^3(N_b{}^5+5N_b{}^4N_t+N_b{}^3N_t(10N_t-3Sy^2)+N_b{}^2N_t(-24$$
$$+10N_t{}^2-9N_tSy^2)+N_bN_t(-72-48N_t+5N_t{}^3+24Sy^2-9N_t{}^2Sy^2)+N_t(-24N_t{}^2+N_t{}^4+24Sy^2$$
$$-3N_t{}^3Sy^2+24N_t(-3+Sy^2)))))-e^{\frac{(N_b+N_t)(h+y)}{h}}y(-24N_b(N_b+N_t)^4(-3h^2Q+h^3U_{HS}+Qy^2-hU_{HS}y^2)$$
$$+Gr_th^3N_b(h^4(-72+N_b{}^3+3N_b{}^2(-4+N_t)+3N_b(-8+N_t)N_t-12N_t{}^2+N_t{}^3)S+24h^3(N_b+N_t)^2Sy$$
$$-12(-2N_b+N_b{}^3-2N_t+3N_b{}^2N_t+3N_bN_t{}^2+N_t{}^3)y^2+2h(N_b+N_t)^3y(12+Sy^2)-3h^2(24N_t-8Sy^2$$
$$+4N_t{}^2Sy^2+N_b{}^3(4+Sy^2)+N_t{}^3(4+Sy^2)+N_b{}^2(4Sy^2+3N_t(4+Sy^2))+N_b(24+8N_tSy^2+3N_t{}^2(4$$
$$+Sy^2))))+Gr_fh^2(h^5N_t(-72+N_b{}^3+3N_b{}^2(-4+N_t)+3N_b(-8+N_t)N_t-12N_t{}^2+N_t{}^3)S$$
$$+24h^4N_t(N_b+N_t)^2Sy-3h(N_b{}^5+5N_b{}^4N_t+2N_b{}^3N_t(2+5N_t)+2N_b{}^2N_t{}^2(6+N_t)+N_t{}^2(-8+4N_t{}^2$$
$$+N_t{}^3)+N_bN_t(-8+12N_t{}^2+5N_t{}^3))y^2+2(N_b+N_t)^5y^3+2h^2N_t(N_b+N_t)^3y(12+Sy^2)+h^3(N_b{}^5$$
$$+5N_b{}^4N_t+N_b{}^3N_t(10N_t-3(4+Sy^2))+N_b{}^2N_t(10N_t{}^2-12Sy^2-9N_t(4+Sy^2))+N_bN_t(-72+5N_t{}^3$$
$$-24N_tSy^2-9N_t{}^2(4+Sy^2)+N_t(-72N_t+N_t{}^4+24Sy^2-12N_t{}^2Sy^2-3N_t{}^3(4+Sy^2))))))\kappa\cosh(h\kappa)$$
$$+24e^{\frac{(N_b+N_t)y}{h}}(-1+e^{N_b+N_t})N_b(N_b+N_t)^4U_{HS}((-3h^2y+y^3)\sinh(h\kappa)$$
$$+2h^3\sin(h\kappa)))(1-\tanh(h\kappa)))/(48(-1+e^{N_b+N_t})h^3N_b(N_b+N_t)^4\kappa).$$

(A13)